FACULTY OF SCIENCE
UNIVERSITY OF COPENHAGEN

Master's Thesis

Cecilie Sand Nørholm

The Effect of Protoclusters on the Properties of Lyman-Alpha Emitters

Supervisors: Dr. Francesco Valentino, Professor Georgios Magdis, Professor Sune Toft

Date of Submission: August 5, 2019

Abstract

The environment surrounding galaxies is a well known driver of their evolution. This is particularly true for galaxies residing in the most overdense environments of the local Universe, namely clusters and groups. However, when and how the environmental effects began playing a role for galaxy evolution is still debated.
In this thesis, we use narrow-band imaging data from the FORS2 instrument at the UT1 Very Large Telescope to identify and study the properties of a sample of 40 Lyman-α emitting galaxies residing in two young cluster progenitors at redshifts z=2.095 and z=2.19, the peak epoch of galaxy assembly. We compare projected number counts of our sample of Lyman-α emitters to values computed from the Lyman-α luminosity functions for field galaxies at similar redshifts as the two protoclusters we examine. Stellar masses and star formation rates are compared to the so-called 'main sequence' of galaxies in the M_*-SFR plane, where the bulk of regular, star forming galaxies are located. We find that within the two protoclusters, the number count of Lyman-α emitting galaxies is lower than expected from the general field of galaxies. Moreover, we find that their star formation rates are below the expected values for field galaxies of same stellar mass. These results indicate that star-forming protocluster galaxies are undergoing early quenching, meaning that they are indeed affected by the surrounding medium, in a similar way to what is observed in local clusters, already 10 Gyr ago.

Furthermore, we investigate whether reservoirs of Lyman-α emitting gas are present in the intracluster medium of the two protoclusters. Though we do not find evidence of extended Lyman-α emission in the central cores of the protoclusters, we discover and spectroscopically confirm a Lyman-α blob, located between a rare pair of active galactic nuclei in the outer region of the z=2.19 protocluster, suggesting a possible connection with the formation of this structure. This shows the power of narrow-band imaging follow-up observations of protoclusters to discover rare systems and it proves the robustness of our analysis, which we plan to expand in the near future by investigating the recently acquired spectroscopy.

Contents

1 Introduction and Motivation

The environment surrounding galaxies is a key factor driving their evolution. However, only recently astrophysicists started exploring the environmental effects in the distant Universe, thanks to improved observational capabilities. When investigating how galaxies are affected by their surroundings, several properties are relevant to include in the analysis. In this thesis we focus on two galaxy protoclusters, searching for galaxies emitting Lyman-α radiation. For these galaxies, we are interested in properties such as number counts, star formation rate, and stellar mass.

This section serves the purpose of introducing the basic concepts of galaxies, galaxy clusters, their evolution, and the nature of observed Lyman-α emission widely used in this thesis. To conclude this section, we describe the research questions which this thesis aims to investigate, while Sections 2 and 3 are dedicated to describe the detection and selection of Lyman-α emitters as well as how we obtain relevant properties of the galaxies in question.

1.1 Concepts of Galaxy Evolution

Galaxies are complex and dynamical systems, changing over timescales of millions, even billions, of years. Such timescales naturally pose a challenge for us humans to understand galaxy evolution, as we are not able to directly observe these changes over such long periods of time.
However, in pursuit of overcoming this challenge, millions of galaxies at different redshifts have been observed in the past few decades. When obtaining observations of the sky, we are able to get a look at a younger universe, as the light from distant galaxies travels towards us with a finite speed. Hence, the travel time for photons emitted by a galaxy depends on the relative distance between this galaxy and our telescopes. This effectively makes it possible for us to look back in time, meaning that by observing objects at different redshifts, we are actually able to inspect galaxies throughout most of the age of the Universe.
Galaxies residing at high redshifts are believed to be the progenitors for the galaxies we observe in the nearby Universe today. However, as we are not physically able to observe how galaxies change over time, we have to use assumptions in order to connect the structures we observe locally and at higher redshifts. Therefore, by

examining galaxies at different redshifts, and thus at different ages of our Universe, we can get some insight in how galaxies evolve over large timescales. When observing galaxies in the nearby Universe, we discover that properties such as their shape, mass, and ability to form stars, seem to be affected by their surrounding environment (see e.g. Dressler [1980] and Balogh et al. [2004]). This poses questions about whether environmental effects have always played the same role in galaxy evolution and when such effects first appeared.
Furthermore, the consequences on the evolution of galaxies being part of galaxy clusters are not very well understood. I will discuss galaxy clusters, their evolution, and their environment further in Section 1.2.

When examining observational data of galaxies, it seems that they can be categorized in two main groups: blue spiral galaxies and red elliptical galaxies. Observations of spiral galaxies reveal disc-like structures containing gas, dust, and star-forming regions along with a more inactive bulge of long-lived stars around the galactic center. Elliptical galaxies, on the other hand, typically have low star formation and are associated with being more mature galaxies. The latter because they contain mainly red stars; either low-mass, long-lived stars or giant stars that have left the stellar main sequence.
These classifications were first made by Hubble [1926], who originally proposed an observational scheme of galaxy morphologies, moving from elliptical galaxies towards 'early' and 'late' type spiral galaxies. Even though we now know this not to be true, it is still thought that there is an evolutionary connection between the spiral and elliptical galaxies. Today we know that galaxy evolution is affected by several parameters; both intrinsic and external. Searching for correlations among physical parameters as a function of their environment allows us to decouple the intrinsic and external drivers of galaxy evolution. An example of such correlation that we will make use of in this thesis is the so called "main sequence" of galaxies relating their stellar mass and star formation rates.

1.1.1 The Galaxy Main Sequence

Star-forming galaxies, both in the nearby Universe and at higher redshifts, have been found to have a strong correlation between their stellar masses and star formation rates [Brinchmann et al., 2004, Daddi et al., 2007, Elbaz et al., 2007, Noeske et al., 2007]. This correlation is referred to as the "galaxy main sequence". This main sequence of galaxies implies that higher stellar mass corresponds to higher star formation rate, as Figure 1.1 shows. The slope of this relation is close to unity and, thus, the relation is nearly linear, with a scatter of $\sim$0.2 dex [Schreiber et al., 2015, Speagle et al., 2014]. While the shape of the main sequence does not change much with redshift, the normalization of this relation increases with increasing redshift. The most massive galaxies have the deepest gravitational potential wells and are thought to reside in the most massive dark matter halos. Hence, these galaxies will naturally accrete and retain more gas and therefore form more stars compared to less massive galaxies, intuitively explaining the existence of the correlation between stellar mass and star formation rate. As the majority of galaxies, at any redshift, are located on the galactic main sequence, this suggests that the evolution of galaxies is dominated by secular processes rather than merger events. This is consistent with the known increase in the cosmic star formation rate density with redshift, up to z∼2, and subsequent decrease beyond this peak [Madau & Dickinson, 2014]. A possible explanation for this could be that younger galaxies have higher fractions of molecular gas, which then depletes over time, reducing the star formation [Magdis et al., 2012, Sargent et al., 2014, Tacconi et al., 2018].

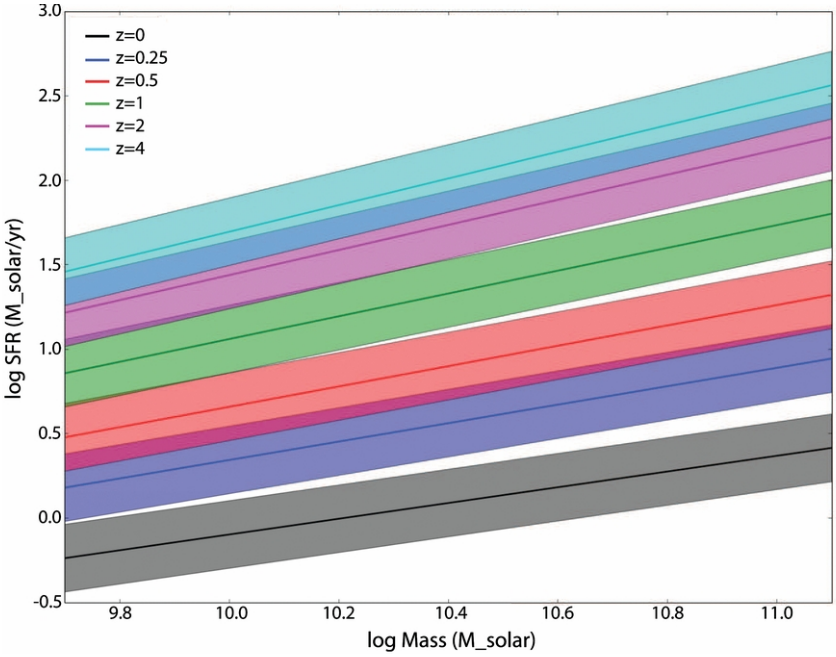

Figure 1.1: Figure from Speagle et al. [2014]. This figure shows the evolution of the galactic main sequence and the dependence on redshift for this M_*-SFR correlation. The normalization of the main sequence increases with higher redshifts, while the overall shape of the correlation stays unchanged.

1.2 Galaxy Clusters

From the moment the first catalogs containing large number of galaxies were published, it was noticed how observed galaxies are seemingly not evenly distributed in space. This observed, web-like structure of matter enclosing large voids [Colless et al., 2001, Gott et al., 1986] is now referred to as the large scale structure of our Universe.

Part of this large scale structure are groups and clusters of galaxies. Galaxy clusters are the most massive, gravitationally bound structures we know of. Their total masses span $10^{14}-10^{15}$ solar masses ($M_\odot$) and they contain up to several hundred galaxies. However, galaxies have been found to only constitute a few percent of the total cluster mass. The observed velocities of galaxies in clusters are too large

to be caused only by mutual attraction between the galaxies, with velocity dispersions of up to 1000 km/s for the richest clusters [Girardi et al., 1993]. Hence, other components must be contributing to the total cluster mass. Observations using X-ray telescopes, such as the Chandra X-ray Observatory, reveal enormous reservoirs of hot gas within galaxy clusters. This intracluster medium can reach temperatures of several million Kelvin, which is why the observed X-ray emission is expected to be due to thermal brehmsstrahlung. Observations of the intracluster medium suggest that the gas mass of a cluster is up to 10 times larger than the mass contribution from galaxies [Sparke & Gallagher, 2007]. The dominant factor of the mass budget in galaxy clusters, however, are neither gas nor galaxies, but dark matter. Though its presence has been known for decades, being first proposed by Zwicky [1933] by measuring the velocity dispersion of the Coma cluster, the nature of dark matter is still unknown. Although we are still unable to detect it, the presence of dark matter is inferred by its gravitational interaction with the surroundings, which can be observed, e.g., through gravitational lensing effects and from the velocity dispersion of galaxies. Hence, it is believed that dark matter is the missing mass component in galaxy clusters, keeping these structures gravitationally bound.
Observations of the low-redshift Universe show galaxy clusters still in the process of collapsing, suggesting that such structures are relatively young. On the other hand, galaxies have been observed at very high redshifts (see e.g. Oesch et al. [2016]), meaning that these must have formed just a few hundred million years after the Universe itself. Such observations strengthen the hypothesis that the dark matter in our Universe is cold (CDM), i.e., the dark matter particles are nonrelativistic when decoupling from other components of the Universe [Ryden, 2003]. Following the ΛCDM model (where Λ refers to the cosmological constant, used in the explanation of the accelerated expansion of our Universe), structures form hierarchically, starting with cold dark matter collapsing in regions with slightly higher density than the surroundings, forming dark matter halos. These halos interact gravitationally with each other, becoming even more massive through merging. Baryonic matter falls into the gravitational potential wells of these dark matter halos, eventually forming the galaxies we observe today.
The definition of a galaxy cluster is not completely settled upon, as the manner of distinguishing groups and clusters of galaxies differ between various studies. For this thesis, I use the definition also adopted by Overzier [2016]; that a galaxy cluster is a virialized object with mass $\gtrsim 10^{14}\, M_{\odot}$. Following from this definition, a protocluster is then defined as a system that will eventually collapse and become a galaxy cluster at present redshift.

In this thesis we will be working on data from two protoclusters: CC0958+0158 located at redshift 2.19 [Strazzullo et al., 2015], and CC1000+0215 located at redshift 2.095 [Kacprzak et al., 2015, Kewley et al., 2016, Spitler et al., 2012, Yuan et al., 2014], which we will refer to as the Strazzullo protocluster and Yuan protocluster, respectively, throughout this thesis. We will introduce these structures in more detail in Section 1.2.4.

1.2.1 Formation and Evolution

The structure we observe in the Universe today is thought to origin from quantum fluctuations in the very early Universe. These fluctuations resulted in small perturbations of the energy density, seen as the slight temperature deviations observed in the cosmic microwave background. Due to gravitational instability, these perturbations have then collapsed and grown over time, by merging, to eventually become the large scale structure of the Universe that we observe today. Figure 1.2 shows the redshift evolution of this large scale structure, as predicted by the Illustris simulation [Vogelsberger et al., 2014].
As matter collapses, to form halos and galaxies, it will at some point settle into an equilibrium. For baryonic matter, this equilibrium configuration is usually described as hydrostatic equilibrium. For dark matter, which is collisionless, this equilibrium can be described by the Jeans equation. The equilibrium state of a galaxy cluster, or protocluster, might be influenced by merging events within the cluster itself or between cluster halos. The latter ultimately leading to growth of these halos, which might affect the properties of the galaxy cluster and the galaxies residing within (see e.g. Kravtsov & Borgani [2012] and references therein).

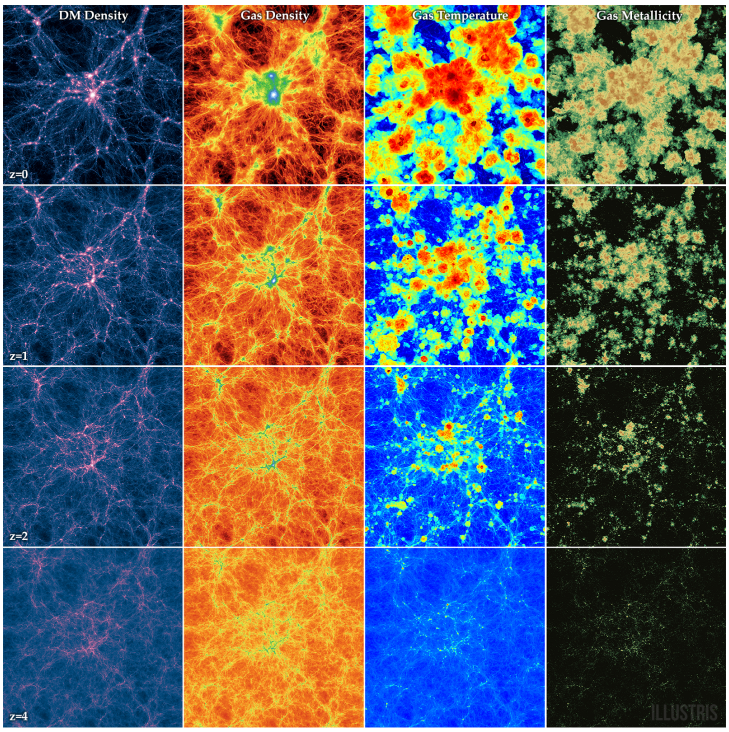

Figure 1.2: A whole box slide from the Illustris simulation, see Vogelsberger et al. [2014], showing the redshift evolution from z=0 to z=4 of the dark matter density, gas density, gas temperature, and gas metallicity, respectively. This clearly illustrates how the filamentary structure of the large scale structure of the Universe becomes more prominent with decreasing redshift, corresponding to increasing age of the Universe. Credit: Illustris Simulation.

1.2.2 Cluster Environments and Their Effect on Galaxies over Time

As mentioned at the beginning of this section, the evolution of galaxies and galaxy clusters is still not fully understood. We know of some factors though, which are likely to affect the properties of clusters and cluster members. Below, we briefly describe the best studied effects of the environment on the evolution of cluster galaxies.

When observing rich clusters, the most luminous galaxies located in the core region are in general red, elliptical and passive, having no spectral features that indicate recent star formation, such as rest-frame UV/optical emission lines from HII regions, far-IR dust emission, or UV light from young, massive stars. A possible explanation for this apparent deficiency of star-forming galaxies might be that cluster galaxies lack cold gas. As galaxies are falling towards the center of a cluster halo, they are thought to lose much of their gas due to ram pressure stripping [Gunn & Gott, 1972] or due to a combination of starvation and gas consumption [Larson et al., 1980]. The former is due to the contrast between the hot intracluster medium and the cooler gas within infalling galaxies, which leads to the development of a shock. This shock causes the gas residing in the interstellar medium (ISM) of this galaxy to be 'left behind', or stripped away, as the galaxy continues to move through the cluster [Gunn & Gott, 1972, Sparke & Gallagher, 2007]. Starvation happens due to the cut of the cold gas accretion onto galaxies, again owing to the presence of hot, intracluster plasma. Through star formation, or supermassive black hole growth, galaxies slowly consume their gas. Hence, both mechanisms for gas removal can explain why we observe red, massive, and passive galaxies in the cores of clusters.

Another factor that triggers abrupt changes in the structure of galaxies are merger events. Even though we reside in an expanding Universe, collisions between galaxies still occur, when the mutual gravitational pull between two galaxies is stronger than the expansion of our Universe. Such collisions between galaxies are expected to be more frequent in regions of overdensity, such as galaxy clusters. The product of a galaxy merger is often elliptical in shape, which can be explained by the stars in galaxy disks being re-arranged into spheroids during, and after, the merging. However, at high redshift, when galaxies are gas rich, mergers often show signs of star-bursts, as the collision between gas rich galaxies result in rapid star-formation. This phase of starburst might be immediately followed by quenching, resulting in a spherical, massive, red, and passive galaxy, as the ones observed in the cores of galaxy clusters [Gómez-Guijarro et al., 2018, Toft et al., 2014].

Merging is not restricted to galaxies only, though. Merging between halos are thought to be the origin of the massive galaxy clusters, e.g., the Virgo and Coma clusters, that we observe today. As a galaxy cluster evolves through merging and infalls, its environment might change. The fact that many galaxy clusters harbour vast reservoirs of X-ray emitting gas shows that radiative cooling is taking place. This cooling, along with feedback from, e.g., supernovae and active galactic nuclei, contributes to the properties of the intracluster medium. This feedback can origin from various mechanisms, though, and it is thus difficult to measure exactly which mechanisms affect the intracluster medium and how they affect it. Nevertheless, we can use the radiation emitted from both the intracluster medium and the galaxies residing in clusters and protoclusters, in order to locate these vast structures. In the next section we describe the most commonly used methods for detecting galaxy clusters.

1.2.3 How to Identify a Cluster of Galaxies

Several techniques are currently available for detecting groups and clusters of galaxies. We will describe some of these techniques here, including the ones used for detecting the Strazzullo- and Yuan protoclusters.

The intracluster medium, as also previously mentioned, is often associated with large reservoirs of hot gas. This gas, reaching temperatures of several million Kelvin, emits X-ray photons via brehmsstrahlung and can therefore be observed through X-ray imaging and spectroscopy, e.g., with the Chandra or XMM-Newton X-ray observatories. Spectral lines from heavy elements in the intracluster medium might also be present in obtained spectra of galaxy clusters. This extended X-ray emission can be used as indicator of cluster environments, and can also be used to estimate the gravitational potential of the cluster, if the gas is assumed to be in hydrostatic equilibrium.
While brehmsstrahlung is thought to be the main source of the X-ray emission measured in the intracluster medium, the thermal electrons causing this emission are also responsible for another, more peculiar, effect. The Sunyaev–Zel'dovich effect, predicted by Sunyaev & Zeldovich [1970], describes how high-energy electrons distorts photons from the cosmic microwave background by inverse Compton-scattering. This effect has been measured by, e.g., the Atacama Cosmology Telescope (ACT) and the Planck Space Observatory, in the search for galaxy clusters. Even though galaxies only contribute with a fraction of the total cluster mass, their emission can also be useful when searching for galaxy clusters. Depending on the redshift, observations from optical or near-infrared (NIR) filters can be used to determine both the colours and the number counts of galaxies. By locating overdensities of galaxies and determining their redshifts, it is possible to estimate whether an overdensity is consistent with clustering. Recently, protocluster cores have also been identified from observations with the Herschel Space Observatory. Bright fluxes measured in the $500\mu m$ channel are thought to originate from several, physically associated objects, located within the wide beam of the telescope. Thus, these measurements can be used to trace clustering of galaxies [Bussmann et al., 2015, Gómez-Guijarro et al., 2019].
Some galaxy clusters have also been observed to have strong radio emission, often present in the central part of the cluster. While extended or diffuse radio emission is often associated with merging clusters, radio emission is also associated with powerful radio galaxies residing in the cluster centers. Thus, radio galaxies can also be used as tracer for protocluster structures at higher redshifts, as described

by e.g. Venemans et al. [2007].
Another method used for detecting galaxy clusters is not dependent on the radiation emitted by the cluster itself, but on emission from galaxies located behind the cluster. Due to their enormous mass, galaxy clusters bend the light emitted by the galaxies behind them, acting as a gravitational lens. By analyzing the distorted images of the lensed galaxies, it is possible to obtain knowledge about the dark matter distribution of the galaxy cluster creating the lensed image.

All these different selection techniques are effective up to different redshift limits and thereby allow us to identify different populations of (proto)clusters at various evolutionary stages. An X-ray or SZ detection requires a relatively massive cluster ($\sim 10^{14}$M$_\odot$) with a warm intracluster medium to be in place. Therefore, such techniques allow us to detect evolved clusters up to a current limit of z$\sim$2-2.5 [Gobat et al., 2011, 2019, Wang et al., 2016]. On the other hand, the use of galaxies as tracers of overdensities can be pushed up to the highest redshifts, with protoclusters detected up to z$\sim$4-6 [Jiang et al., 2018, Overzier, 2016] However, these structures are still in the phase of assembly and are much younger than the clusters we observe in X-ray or through the SZ effect. Therefore, it is important to specify the selection technique used to identify a (proto)cluster, since this strongly affects the results on the effect on their members.

In this thesis, we explore yet another possible detection method, as we investigate whether Lyman-α emission can be used to effectively trace or confirm galaxy overdensities at z$\sim$2 [Overzier, 2016].

1.2.4 Protoclusters in This Thesis

As mentioned above, there are several methods for detecting galaxy clusters and protoclusters. In this section we briefly describe how the Strazzullo and Yuan protoclusters are identified as well as some of their properties.
Strazzullo et al. [2015] use BzK-colours [Daddi et al., 2004] to isolate overdensities of red, passive galaxies in the COSMOS field [Scoville et al., 2007], as clusters are expected to contain a higher fraction of quiescent galaxies compared to low-density environments (e.g., due to removal of cold gas from the galaxy ISM). Due to this choice of tracer, Strazzullo et al. [2015] expect to be biased towards more evolved structures. Using the 5^{th} nearest neighbour algorithm (see Figure 1.3) they identify a concentration of four passive galaxies within 130 kpc, all consistent with having passive UVJ-colours in the catalog by Muzzin et al. [2013a]. Partial confirmation of this structure is achieved by combining zCOSMOS [Lilly et al., 2007] and Valentino et al. [2015], who confirmed a few star-forming objects at a consistent z$\sim$2.19 redshift via spectroscopy. The central coordinates of this overdensity are reported to be $RA \sim 09{:}58{:}53$, $DEC \sim +01{:}58{:}01$. Strazzullo et al. [2015] predicts that this structure is not reachable by either Chandra or XMM-Newton, which poses upper limits of $\sim 5-7 \cdot 10^{13}$M$_\odot$ on the protocluster mass and $\sim 4-9 \cdot 10^{43}$ erg s^{-1} on the X-ray luminosity.

Yuan et al. [2014] identify several surface density peaks using overdensities of blue, star-forming galaxies. The overdensity was first traced using near-IR [Spitler et al., 2012], see Figure 1.4, however Yuan et al. [2014] use spectroscopy from the MOSFIRE instrument, which is biased towards star-forming galaxies. They obtain spectroscopy of 180 objects, of which 57 is consistent with the adopted redshift of the Yuan protocluster (z=2.095). Nearest neighbour algorithms are used to identify 4 surface density peaks, referred to as A, B, C, and D. These peaks are centered on the position of 4 massive (>10^{11} $M_\odot$) galaxies in the region of the overdensities, with the median position of the protocluster members located at $RA: 10:00:22.646$, $DEC: +02:15:05.91$. As the Yuan protocluster has several surface density peaks and, thus, are less compact than the Strazzullo protocluster, we expect that this structure is still in the process of merging and that it is therefore the youngest of the two protoclusters.

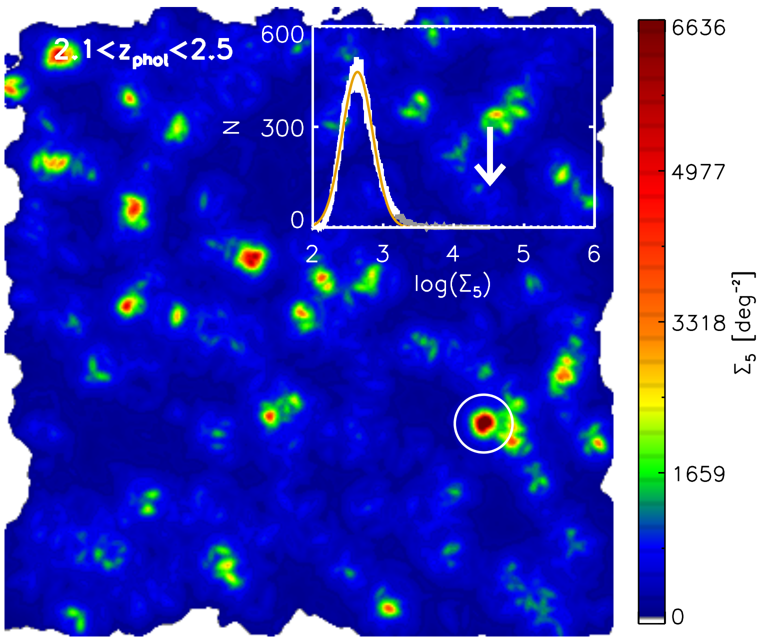

Figure 1.3: Figure from Strazzullo et al. [2015] showing the 5^{th} nearest neighbour surface density map for the overdensity of red, passive galaxies in a photometric redshift interval of 1.5<z<2.5. Strazzullo et al. [2015] finds that a peak in surface density is present at a spectroscopic redshift of 2.19. The narrow-band observations of the Strazzullo protocluster are centered on the central coordinates of this overdensity.

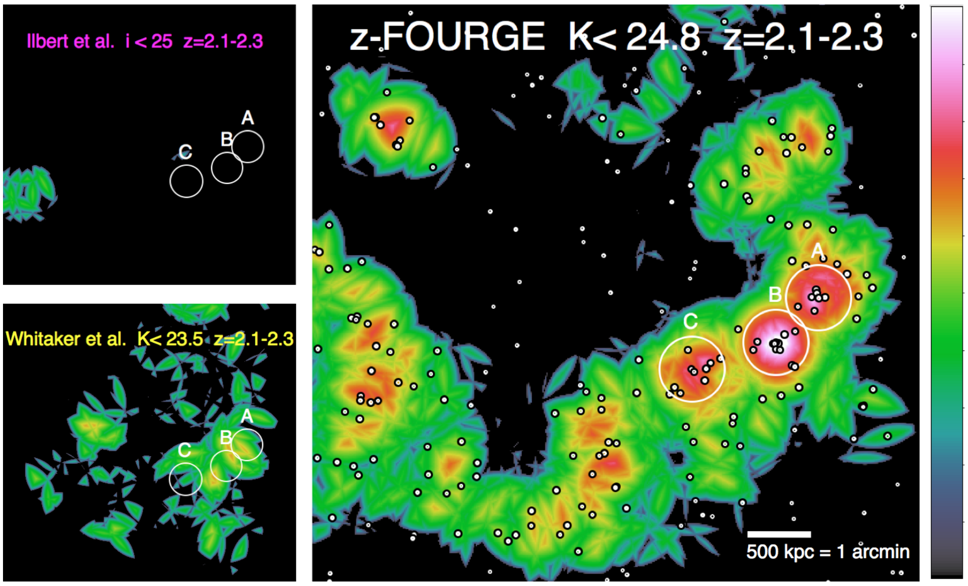

Figure 1.4: Figure from Spitler et al. [2012] showing the 7^{th} nearest neighbour surface density maps of the region covering the Yuan protocluster in the redshift interval $2.1 \leq z \leq 2.3$. This overdensity is initially identified through deep near-IR photometry, while Yuan et al. [2014] use spectroscopy targeting star-forming objects. Surface density peaks A, B, and C are marked on this map. Yuan et al. [2014] identify another surface density peak, D, located above surface density peak A.

1.3 Lyman-alpha

The Lyman-series, and especially the Lyman-α spectral line, serves as a powerful tool for observing our Universe. Originating from transitions in atomic hydrogen, the most abundant element in the Universe, the spectral features of the Lyman-series are expected to be observable throughout the cosmos. The Lyman-α spectral line, written as Lyα from here on, is the result of an electron transitioning from the 1^{st} excited state to the ground state of a hydrogen atom. Lyα photons are emitted at a wavelength of 1215.67 Å, corresponding to the photons having an energy of 10.2 eV, which is exactly equal to the energy difference between the ground state and first excited level.

The emission of Lyα is powered by collisional excitation or photoionization. Collisional excitation of a hydrogen atom happens through interaction with a free electron, where thermal energy of the electron excites the electrons of the hydrogen atom. Hence, the thermal energy of the free electron is converted to Lyα radiation when the excited electron falls back into the ground state, ultimately leading to cooling of the gas.

Recombination of a proton and an electron, following photoionization, might also result in the emission of a Lyα photon. Hydrogen can be created by a free proton capturing a free electron, though this recombination might not necessarily result in the electron directly being in the ground state. Atoms excited after recombination de-excites through radiation, creating photon cascades, which for hydrogen include the emission of Lyα photons in a large fraction of the cases [Spitzer, 1978].

Lyα spectral lines have several uses in modern astronomy. While useful for determining spectroscopic redshifts of galaxies, Lyα emission is also used for exploring the distribution of gas throughout our Universe. By studying spectra from distant quasars, several Lyα absorption features can be observed. These features, dubbed the 'Lyα Forest', reveal how clouds of gas and dust are present at different redshifts, as these affect the radiative transfer of the Lyα emission (see Dijkstra [2017] and references therein). The resonant nature of the Lyα photons means that they are easily scattered on neutral hydrogen or absorbed by dust particles, which is the reason that we are able to observe the Lyα forest in the first place. Thus, the complex radiative transfer of Lyα can cause difficulties when using Lyα emission for estimating physical parameters of, e.g., galaxies, as the escape fraction of Lyα photons must be quite small.

Lyα radiation is thought to be most prominent within the interstellar medium of galaxies. When newly formed, hot, massive O-type stars emit ionizing photons, which are then absorbed by the surrounding medium, ionized HII regions are created. Recombination of free protons and electrons in these regions cause the emission of spectral lines, such as Lyα and Hα. Thus, Lyα emission can be used as tracer of physical parameters, such as star formation. These parameters can provide further information about the galaxies emitting Lyα radiation. We briefly describe such galaxies, and other sources of Lyα emission, below.

1.3.1 Lyman-Alpha Emitters

As mentioned above, one of the main sources of Lyα photons are star-forming regions in the ISM. Due to this fact, Lyα emitters are often associated with being star-forming galaxies. Furthermore, Lyα emitting galaxies are also associated with being relatively young and are, thus, thought to be low-mass objects [Gawiser et al., 2007] with low dust content [Venemans et al., 2005].

Because of Lyα radiation being easily absorbed or scattered by dust or neutral gas, we expect to observe the strongest Lyα emission from objects with only a small amount of dust. Such galaxies should in general appear bluer, due to ongoing star formation and thus, the presence of O- and B-stars, but also due to the lack of obscuration and thermal emission from dust. This would also be consistent with the escape fraction of Lyα photons being larger at higher redshift, possibly due to the dust content in the ISM of galaxies increasing over time [Hayes et al., 2011].

Star-forming galaxies are not the only Lyα emitting objects, though. Active galactic nuclei (AGN) are also observed to have significant amounts of Lyα emission. AGN are characterized by their strong emission over the whole electromagnetic spectrum, which is believed to be caused by the accretion of material onto the central black hole of the galaxy. This accretion causes the gas to heat up and generates emission, which leads to a decrease in potential energy of the gas, causing it to move to orbits closer to the black hole. When the powerful, ionizing emission from this accretion disk reaches the hydrogen in the surrounding medium,

it triggers photoionization and thereby the production of Lyα photons, through recombination, as described above.
Thus, Lyα emission in galaxies can be generated in a variety of environments and, thus, it depends on multiple parameters, meaning that we cannot assume Lyα emitting objects to be described by a single and homogeneous population of galaxies.

1.3.2 Narrow-band Imaging Technique

In this thesis, we make use of the narrow-band imaging technique to retrieve measurements and maps of Lyα emission within the Strazzullo and Yuan protoclusters. Figure 1.5 illustrates this technique of combining measurements from broad- and narrow-band filters. Broad-band filters are useful for capturing the continuum of an object or area on the sky. However, spectral lines can be tricky to isolate with broad-band filters, due to the large range of wavelengths covered by these. Narrow-band filters, on the other hand, are designed for the purpose of observing emission (or lack of thereof) at specific wavelengths only. Their narrow wavelength coverage is ideal for capturing spectral line emission, though measurements of the continuum can be difficult.
The right panel of Figure 1.5 shows how we use broad- and narrow-band filters to isolate Lyα line emission. We subtract the continuum, mainly measured in the broad-band filter, from the narrow-band measurements, resulting in measurements of the line emission. The image in the top left corner of each panel is showing how continuum and line flux, respectively, contributes to the detection of emitters.

We will expand this intuitive description of the technique in Section 2, providing the tools to derive the line and continuum fluxes from the combination of narrow-band and broad-band imaging.

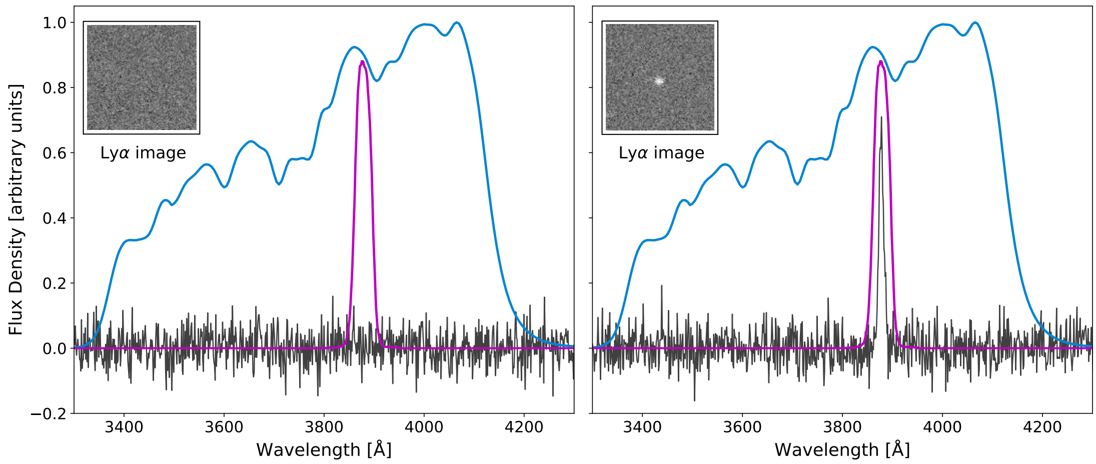

Figure 1.5: Synthetic continuum and emission spectrum (black), to illustrate the advantage of using narrow-band observations. The broad-band filter (blue) covers a wide wavelength range and captures the continuum well, while the narrow-band filter (pink) is designed to capture emission lines and, thus, covers a much shorter wavelength range. For display purposes only.

1.4 This Thesis

This thesis is aimed at investigating whether Lyα emitting galaxies within two overdensities, the Strazzullo and Yuan protoclusters, are affected by the surrounding environment. This question is naturally followed by *how* the protocluster environment then affects these galaxies. As we aim to examine several properties of the protocluster members, we strive to determine which parameters are affected the most by the overdense surroundings.
In short, this thesis is aimed at investigating the following:

- The environmental effects on the evolution, and the properties, of star-forming galaxies in two protoclusters at different evolutionary stages.
- The stellar masses and star formation rates of star-forming galaxies within protoclusters, and how these properties compare to the stellar mass-star formation rate relation for typical objects residing in low-density field environments.
- The projected number counts of Lyα emitting protocluster galaxies and how these compare with expected values for the general field of galaxies.

In details, during this project we have worked on reducing and analyzing narrow-band imaging data, recently acquired from the FORS2 instrument mounted on the Very Large Telescope. Using these data, we identify emission of the hydrogen Lyα transition.
Empirical and statistical tools are used to retrieve the main properties of individual galaxies in the Strazzullo and Yuan protoclusters. These properties include projected number counts, star formation rates, stellar masses, dust obscuration, and

spatial distribution. The retrieved properties are then compared with the equivalent counterparts in low density environments, so to detect possible effects on the evolution of a galaxy, due to the presence and evolutionary stage of surrounding massive structures.

While the focus of this thesis is on the environmental effects on galaxy evolution, we also have the opportunity to explore the presence of a young intracluster medium. Specifically, we can search for evidence of cold gas in the intracluster medium, as this gas, when ionized, is expected to emit Lyα photons. Therefore, the final part of this thesis is dedicated to the search of extended Lyα emission between protocluster members. However, this part of our work should be intended as preliminary and as a base for future developments, described in the last chapter of this thesis. Such future developments have already started with a spectroscopic follow-up of a rare QSO-pair in the Strazzullo protocluster, confirming the validity of our approach and analysis.

2 Methods

This section briefly describes the methods used for obtaining properties of the detected Lyα emitters in the Strazzullo and Yuan protoclusters. These properties include Lyα emission line fluxes, line equivalent widths, continuum fluxes, star formation rates, and stellar masses.
The nature of the detected Lyα emitters is described in Section 4.

2.1 Measuring Lyman-alpha Emission

Narrow-band filters are often used for observations, when specific spectral lines are targeted. However, even though a narrow-band filter is well-suited for isolating light from emission lines, the measured flux will still be a combination of emission from continuum and spectral lines. The flux emitted by an object can be expressed in the following way:

$$F = \int F_\lambda \, d\lambda \tag{2.1}$$

Where F_λ is the flux density per unit wavelength; i.e., the spectrum. This spectrum will have contributions from both continuum emission and spectral lines, regardless of whether observations are made with a broad-band or narrow-band filter. If we now assume that the spectrum has a flat continuum and an infinitely narrow emission line at wavelength λ_0, we can write F_λ as:

$$F_\lambda = c(\lambda) + F_{em}(\lambda) \cdot \delta(\lambda_0) \tag{2.2}$$

Where $c(\lambda)$ is the continuum flux, F_{em} is the flux of the spectral line, and $\delta(\lambda_0)$ is a delta function describing the spectral line at a specific wavelength. In this case we are focusing on emission lines. Throughout this thesis we use wavelengths in units of Angstrom, fluxes in units of erg cm^{-2} s^{-1} and, thus, flux densities in units of erg cm^{-2} s^{-1} Å^{-1}.
The assumptions behind eq. 2.2 are somewhat consistent with what we expect from our observations. We expect the width of the Lyα emission line to be much narrower than the narrow-band filters we use, thus, approximately a delta-fuction. Additionally, the central wavelengths of our narrow-bands are very close to that of the used broad-band. Hence, we expect little to no variation in the continuum flux density between the central wavelengths of the adopted filters. This allows us

to use the flat continuum approximation around the wavelength of the emission line.

The bandpass signal in a given filter is not only dependent on the flux, but also on the throughput of the filter. In order to take this throughput into account, we can define an 'effective width' of a filter. This effective filter width is given as the integral of the transmission over the wavelength range covered by the filter, weighted by the transmission at the expected wavelength, λ_0, of the emission line.

$$\varepsilon_x = \frac{\int x(\lambda)\, d\lambda}{x(\lambda_0)} \tag{2.3}$$

Where $x(\lambda)$ describes the filter transmission at the instrument and telescope used.

The bandpass, i.e., the flux density, in the filter x is then defined as:

$$F_x = \frac{\int F_\lambda \cdot x(\lambda)\, d\lambda}{\int x(\lambda)\, d\lambda} \tag{2.4}$$

2.1.1 Line Emission

Following Bunker et al. [1995], we use broad- and narrow-band measurements to find continuum fluxes, emission line fluxes, and equivalent widths.

Combining Measurements from Broad- and Narrow-band Filters

As we also describe in Section 1.3.2, observations of the Strazzullo and Yuan protoclusters are obtained using narrow-band filters. These narrow-band frames are then reduced, background-subtracted, and combined into a final science frame for each protocluster (see Section 3).
The reduced science frames are used together with broad-band imaging covering the protocluster areas, in order to obtain photometry of the objects in the frames. By using the coordinates of objects detected in the broad-band frame, flux measurements are extracted in both the broad-band and narrow-band frames. Comparing these measurements, e.g., by creating a colour-magnitude diagram (see Figure 3.3), will then make it possible to determine if any objects have significant narrow-band excess or absorption. Using the same approach as Bunker et al. [1995], narrow-band and broad-band measurements, as well as information about the filters, are used to determine Lyα emission line fluxes, line equivalent widths, and continuum fluxes.

Lyman-alpha Line Emission

Using the definition of flux density, described in eq. 2.4, we can derive the emission line flux. As mentioned above, the flux of an object initially has contributions from both continuum and line emission, so in order to isolate the emission line flux, we need to correct for the continuum. This we can do by using the broad-band emission and taking the effective filter widths into account [Venemans et al., 2005]. Eq. 2.5 shows how we use information, i.e., effective filter widths and flux densities, from both the broad- and narrow-band filter to obtain the flux of the emission line:

$$F_{em} = \frac{\left(F_U - F_{NB}\right) \cdot \left(\varepsilon_U \cdot \varepsilon_{NB}\right)}{\left(\varepsilon_{NB} - \varepsilon_U\right)} \tag{2.5}$$

In the above equation, F_U and F_{NB} are the flux densities measured in the u broad-band and narrow-band, respectively.
The emission line fluxes are used not only to obtain physical parameters, such as star formation rates, for the emitting sources, but also to determine the equivalent widths of the emission lines. However, in order to be able to determine the equivalent width of an emission line, we also need to know the continuum flux emission. The latter is described in the following section.

2.1.2 Continuum Flux

By isolating $c(\lambda)$ and substituting the expression for F_{em} (eq. 2.5) into eq. 2.2, we obtain an expression for the continuum emission:

$$c_{\lambda_0} = \frac{\varepsilon_{NB} \cdot F_{NB} - \varepsilon_U \cdot F_U}{\left(\varepsilon_{NB} - \varepsilon_U\right)} \tag{2.6}$$

Eq. 2.6 describes the continuum at wavelength λ_0. If we define λ_0 as the observed wavelength of a specific emission line, e.g., Lyα, then eq. 2.6 will be the corresponding continuum emission underlying this emission line.

2.1.3 Equivalent Width

We compute the equivalent width of the emission, eq. 2.7, by combining eqs. 2.5 and 2.6. The equivalent width is originally defined to have positive values for absorption lines and negative values for emission lines. However, since this thesis will only focus on emission lines, we use positive values of the equivalent widths, for simplicity and consistency with common usage in the literature.

$$EW = \frac{F_{em}}{c_\lambda} \tag{2.7}$$

In equation 2.7, F_{em} is the emission line flux and c_λ is the continuum flux density at the central wavelength of the emission line. Since we have expressions for both components in eq. 2.7, we can rewrite the equivalent width as:

$$EW = \frac{\left(F_U - F_{NB}\right) \cdot \left(\varepsilon_U \cdot \varepsilon_{NB}\right)}{\varepsilon_{NB} \cdot F_{NB} - \varepsilon_U \cdot F_U} \tag{2.8}$$

The resulting equivalent widths are expressed in units of Angstrom, following that fluxes are in cgs units and effective filter widths are also in units of Angstrom.

2.2 Measuring Star Formation Rate

Star formation rates are important when investigating the evolution of galaxies. The formation of stars contributes to processes such as the depletion and ionization of gas, formation of dust, and the assembly of stellar mass of a galaxy. These are all parameters playing a role in galaxy evolution, which is why we are interested in examining if the star formation rate of a galaxy is affected by the surrounding environment.

The star formation rate, SFR from here on, describes the mass of stars formed over a period of time, customarily expressed in units of solar masses per year ($M_\odot\, yr^{-1}$). It should be noted that SFR is a measure of the ongoing conversion of gas into stars, averaged over a timescale of typically 5-100 Myrs. This timescale is dependent on the tracer used; Lyα (and Hα) works as a proxy for the ionizing emission from O-stars, and hence these lines are sensitive to star formation on timescales of 5-10 Myr. UV and far-IR emission are sensitive to star-formation over longer timescales, as UV is also affected by emission from B-stars, and the far-IR tracks thermal dust emission.

When we instead mention the star formation history, SFH, of a galaxy, this describes SFRs as function of time. By integrating the SFH over time, it is possible to obtain the stellar mass (not taking mass loss into account), as this corresponds to the total amount of stars formed in a galaxy. In this section we describe the methods we use to estimate SFRs from Lyα and UV flux measurements.

2.2.1 SFR From Lyman-alpha Emission

Lyα emission is often associated with star-forming galaxies, as described in section 1.3. As the formation of stars is in itself a complex process, there is not just one single indicator of star formation in galaxies. A direct way of tracing instantaneous star formation is by measuring the amount of ionizing photons ($\lambda < 912$ Å) emitted by the most massive stars (O- and early-type B-stars). This emission is also referred to as the Lyman continuum, or LyC. LyC photons are difficult to observe, though, as most of these are either absorbed by neutral hydrogen atoms, creating the ionized HII regions, or destroyed by dust grains. However, Lyα emission functions as tracer of the LyC photons, as recombination of ionized hydrogen is likely to result in the emission of Lyα photons (see Section 1.3), meaning that we can use the Lyα luminosity to estimate the SFR of a star-forming galaxy.

In the case of both LyC and Lyα, we need intrinsic quantities in order to be able to compute meaningful SFRs. This is why escape fractions, f^{esc}, become relevant, as typically only a few percent of the Lyα- and ionizing photons escape from star-forming galaxies, due to both LyC and Lyα photons being prone to absorption or scattering. Thus, we need to take these escape fractions into account, when estimating the SFR of a galaxy. Following Sobral & Matthee [2019], assuming a Chabrier [2003] IMF, we use the following expression for SFR from Lyα emission:

$$SFR_{Ly\alpha}\,[M_\odot\, yr^{-1}] = \frac{4.4\cdot 10^{-42}}{\left(1-f^{esc}_{LyC}\right)}\cdot\frac{L_{Ly\alpha}}{8.7\cdot f^{esc}_{Ly\alpha}} \tag{2.9}$$

The escape fraction of Lyα photons can be estimated by comparing the observed Lyα luminosities, $L_{Ly\alpha}$, and the intrinsic luminosity. The latter can be derived from the intrinsic, dust corrected Hα luminosities, $L_{H\alpha}$, by applying a constant factor of 8.7. This value origins from case B recombination, typical of HII regions (see e.g. Osterbrock & Ferland [2006]). Inverting the argument; if we know $L_{Ly\alpha}$ and the escape fraction, then this relation can be used as an expression for the intrinsic $L_{H\alpha}$, which is useful as $L_{H\alpha}$ is in itself a well-known tracer of SFR [Kennicutt, 1998]. The escape fraction of LyC photons, f_{LyC}^{esc}, is a minimal correction to account for the energetic photons which escape the galaxy without ionizing the surrounding gas. At this stage, f_{LyC}^{esc} is negligible and will thus assumed to be zero.
The resulting SFRs are dust corrected quantities, even though we use the observed Lyα luminosity. This is due to the escape fraction of Lyα photons being defined using the dust corrected $L_{H\alpha}$.

Dependency on Equivalent Width

Sobral & Matthee [2019] find a correlation between $f_{Ly\alpha}^{esc}$ and the rest-frame equivalent width of the Lyα emission line. Through fitting to this correlation, they obtain the following relation:

$$f_{Ly\alpha}^{esc} = 0.0048 \cdot EW_0 \ \pm \ 0.05 \tag{2.10}$$

Where the restframe equivalent width, EW_0, is given by:

$$EW_0 = \frac{EW}{(1+z)} \tag{2.11}$$

Eq. 2.10 is valid for values of EW_0 up to $\sim$160 Å, but might also be usable for slightly larger EW_0. However, for rest-frame equivalent widths above 210 Å, $f_{Ly\alpha}^{esc}$ is expected to be close to 100%.

If we substitute eq. 2.10 into eq. 2.9, we can write the SFR from Lyα emission as:

$$SFR_{Ly\alpha} = \frac{4.4 \cdot 10^{-42}}{\left(1 - f_{LyC}^{esc}\right)} \cdot \frac{L_{Ly\alpha}}{0.042 \cdot EW_0} \tag{2.12}$$

It should be noted that eq. 2.12 tends to overestimate SFRs for galaxies with low star formation ($\leq 40\ M_{\odot}\, yr^{-1}$). For objects selected based on their UV emission, as in our case, eq. 2.12 also predicts higher SFRs by a factor of 0.23 dex, compared to SFRs found through UV luminosity [Sobral & Matthee, 2019]. We will return to this point when presenting our results (Section 4).

2.2.2 SFR from UV-luminosity

As previously mentioned, ultraviolet emission from the most massive stars can be used as an indicator of the SFR of a galaxy. In this thesis, we use the expression for

SFR described by Kennicutt [1998] to estimate SFRs from UV luminosity (1500-2800 Å):

$$SFR_{UV} = \frac{1.4 \cdot 10^{-28} \cdot L_{UV}}{1.795} \tag{2.13}$$

Where the factor of 1.795 is a conversion used when going from a Salpeter [1955] IMF to a Chabrier [2003] IMF.
Luminosities, both $L_{Ly\alpha}$ and L_{UV}, are computed using the inverse square law with flux and luminosity distance. Throughout this thesis, we will be using eqs. 2.12 and 2.13 when determining star formation rates (see Section 4.4).

2.3 Stellar Masses

We estimate stellar masses, M_*, using emission from the rest-frame optical spectrum, as this traces the long-living stars, which dominate the stellar mass budget in galaxies. However, to be able to convert such emission to mass, we will need a mass-to-light ratio. In this case we derive a first, and simple, estimate of M_* by converting the observed K-band luminosity, as in Arnouts et al. [2007]:

$$M_* = \big(-0.27 \cdot z \cdot -0.05 \big) \cdot L_K - 0.24 \tag{2.14}$$

Where L_K is the luminosity in the K-band and z is the redshift.
The mass-to-light ratio from Arnouts et al. [2007] is expressed as a power law, where the coefficients presented in eq. 2.14 are valid for blue galaxies.

2.4 SED-Fitting

In the above sections, we are using empirical relations for obtaining SFRs and M_* of galaxies from single-band or line observations. However, another powerful tool for collecting information about galaxies is by modeling their whole photometric information or spectral energy distributions (SEDs).
Various methods are available for performing such SED-fitting. We derive a second estimate of M_*, using the whole SED information (and not only the K-band luminosity, see Section 2.3), SFR, and dust attenuation as described in Strazzullo et al. [2015] and Valentino et al. [2015].
Dr. Veronica Strazzullo[1] has provided catalogs of M_*, SFR, and extinction (A_V) with two different configurations of the star formation history: constant star formation and exponentially delayed star formation [V. Strazzullo private communication]. These catalogs are using Bruzual & Charlot [2003] models, with a Chabrier [2003] IMF. Dust extinctions are estimated using the Calzetti et al. [2000] reddening law. We will use SFRs from the SED-fitting catalog obtained using constant star formation history. We do so, as it produces SFRs consistent with estimates derived from other tracers, e.g., Hα flux [Valentino et al., 2015], despite being an

[1]Department of Physics, Ludwig-Maximilians-Universität, Scheinerstr. 1, 81679 München, Germany

obvious simplification of the real SFH of a galaxy, especially in its youngest phases. The M_* we use, on the other hand, are from the catalog made using the configuration of exponentially delayed star formation. We make this choice, as the cosmic star formation history shows a peak in SFR around z$\sim$2 (see, e.g., Madau & Dickinson [2014]), hence an exponentially delayed SFH gives a better representation of the assembly of stellar mass in star-forming galaxies, compared to constant SFH.

3 Data Processing

This section presents an overview of the data underlying this thesis, as well as describes the collection and reduction of photometric narrow-band data from the FORS2 (FOcal Reducer and low dispersion Spectrograph) instrument, part of the UT1 Very Large Telescope located at Cerro Paranal, Chile.

3.1 Data Overview

The data which the work in this thesis is based upon, consist mainly of narrow-band imaging, described in Section 3.1.1, as well as imaging from the u-band of the MegaCam instrument at the Canada-France-Hawaii 3.6 meter Telescope (CFHT). Softwares such as Source Extractor [Bertin & Arnouts, 1996] can be used to obtain information by detecting sources and extracting photometry from this imaging data. However, additional information about the detected objects is required. We collect this information from available catalogs and through fitting to the spectral energy distribution of detected objects, the latter kindly provided by Dr. Veronica Strazzullo.

We collect photometry in the following bands: u (CFHT), $BVgriz$ (Subaru), and $YJHK$ (UltraVISTA) from the catalog by Muzzin et al. [2013a], while photometric redshifts are collected from the COSMOS 2015 catalog [Laigle et al., 2016]. Properties such as stellar masses, star formation rates, and V-band extinction are obtained through SED-fitting (see Section 2.4), where the fitting includes the above bands as well as the 3.5 and 4.5 μm IRAC-channels (*Spitzer*).

3.1.1 Narrow-band Imaging Data

The narrow-band imaging data used in this project have been obtained with the FOcal Reducer and low dispersion Spectrograph (FORS2) instrument, mounted on the UT1 VLT (098.A-0244(A), PI: Francesco Valentino). The obtained data cover 2 galaxy protoclusters at different evolutionary stages and consists of 42 frames; 18 covering the Strazzullo protocluster at z=2.19 and 24 covering the Yuan protocluster at z=2.095 (see Section 1.2). These frames are divided between the 2 CCD chips of the FORS2 instrument.

The photometric narrow-band data are accessed through the ESO Science Archive

Facility[2] and consist of calibration frames, in our case bias- and flat field-frames, as well as the actual observations of the Strazzullo and Yuan protoclusters.
The frames covering the Strazzullo protocluster are obtained with 3 hours of observation using the FILT388+4 narrow-band filter, while the Yuan protocluster is observed for 4 hours using the OII/4000+45 narrow-band filter. The frames of the Strazzullo protocluster cover a region of ~9.7x7.8 arcminutes, which at z=2.19 corresponds to an area of ~18.5 Mpc^2. Frames covering the Yuan protocluster cover an area of ~7.4x7.8 arcminutes, corresponding to an area of ~14.5 Mpc^2 at z=2.095. As galaxy clusters at z~0 can be observed to span a few Mpc across, our narrow-band frames should be able to cover the area of a protocluster structure at z~2. The narrow-band filters have widths of 40 Å and 65 Å, respectively. Transmission curves of the filters are shown in Figure 3.1. The observations of both protoclusters were carried out between February 20, 2017 and February 21, 2017 with average seeing conditions of 0.925" (FWHM) during the night.

3.2 Data Reduction

In general, the reduction of observational data consists of several steps for correcting, cleaning, and calibrating the frames. These steps are taken in order to obtain a final science frame with high signal-to-noise ratio and without unwanted effects, such as, e.g., fringing or cosmic ray hits.
This is usually done by using bias- and flat field-frames, with our data being no exception from this. This section describes the reduction of the observational data for the Strazzullo and Yuan protoclusters, from raw frames to the final product: the combined, flux- and astrometrically calibrated science frames.

3.2.1 EsoReflex

Several of the instruments at the European Southern Observatory, FORS2 included, have available reduction pipelines. These pipelines provide tools to perform data reduction through an environment developed to automatize the reduction process. For this thesis, the EsoReflex pipeline is used for the initial reduction of the data. This includes the creation of master frames for the bias and flat fields, normalization of the master flat field, and bias and flat-field correction of the science frames.
One advantage of using the EsoReflex pipeline is that it also produces corresponding noise maps for each reduced science frame, which can be used as weights when combining these frames (see Section 3.2.4).

3.2.2 Cosmic Ray Cleaning

When conducting observations of long exposure times, the presence of high energy particles, from here on referred to as cosmic rays, is inevitable.
Since such cosmic ray events are in most cases instantaneous and randomly hit the

[2]`http://archive.eso.org/cms.html`

detectors, it is unlikely that the same pixels in several exposures will be affected by cosmic rays. This provides a way of 'correcting' the contaminated pixels, by replacing the values of these pixels with values from corresponding pixels in another exposure of the same area on the sky. However, in order to correct an exposure for cosmic ray hits, we first have to detect such events. This can be done either by using the contrast between the pixels contaminated by cosmic rays and the pixels surrounding these, or by focusing on the sharpness of the affected pixel edges.
We apply the latter method on the data used in this thesis. To do so, we are making use of the Laplacian Cosmic Ray Detection algorithm, LAcos, which identifies cosmic rays by using the Laplacian of a two-dimensional Gaussian function [van Dokkum, 2001]. The LAcos cosmic ray cleaning algorithm is applied to the bias-subtracted and flat-field corrected frames with the parameter values presented in Table 3.1.

Table 3.1: LAcos Parameters

Protocluster	Strazzullo	Yuan
Detection threshold [σ]	3.5	3.5
Fractional detection threshold for neighbouring pixels [σ]	0.5	0.2
Contrast limit between cosmic rays and underlying objects [σ]	1.5	0.5
Number of iterations	5	7

Parameters for the LAcos cosmic ray cleaning algorithm, when used on our reduced science frames of the Strazzullo and Yuan protoclusters.

The use of the Laplacian algorithm is quite effective in cleaning the reduced frames for cosmic rays. However, one disadvantage of using the LAcos algorithm is that the processing time increases with the size of the frames to be cleaned. As a consequence of this, it is possible to get to a point where a decision has to be made about whether a higher number of iterations will give a satisfying result, in comparison to the amount of time required to run the algorithm.
Besides the processing time, a higher number of iterations will at some point begin replacing the brightest pixels of, e.g., stars. This is of course undesirable, as real flux values will then be affected by the cleaning.
In order to get the right balance between cleaning and processing time, we tried several approaches and found that the number of iterations given in Table 3.1 results in an acceptable cleaning of the frames, while still maintaining a reasonable processing time.

3.2.3 Super Flat Frames

During observations, flat field-frames are always obtained in order to correct the observations for gradients or other artificial effects that might affect the science frames. However, since we are interested in detecting very small flux excesses with

respect to the background, we apply a second order correction to the flat field by creating a super flat field. The purpose of such a frame is to minimize large-scale variations and gradients in the science frames.
The super flat field-frames, from now on referred to as super-flats, are created by carefully combining bias- and flat field-corrected science frames. We initially normalize each frame by its own median background level and mask out the bright sources to avoid their contribution to the background. We use the segmentation map created by the Source Extractor software [Bertin & Arnouts, 1996] as a mask, downweighting the pixel values of the bright sources. We then stack the normalized, source-free frames together. We use median stacking as this rejects possible outliers in the sky flux distribution. We also apply a 5σ clipping to ensure that strongly deviating pixels are removed. The result of the combined, masked frames is a normalized super-flat, which contains only the structure present in the 'blank' sky. Finally, we subtract this super-flat from the individual science frames after properly matching their background level. This method works because of the large dithering pattern applied during the observations, so that any source never covers the same area of the detector for more than a minor fraction of the integration time.

3.2.4 Combination of the Reduced Science Frames

The conclusive goal of the whole data reduction process is to create one final, reduced, background subtracted, and cosmic ray cleaned science frame for each observed object or area on the sky. The final step towards this goal is, in our case, to combine all of the reduced exposures for the Strazzullo and Yuan protoclusters. We use the SWarp software [Bertin et al., 2002] for the coaddition of our reduced science frames. One of the benefits of using SWarp is that the software is capable of performing a weighted combination of frames. A weighted combination is desired if, as in our case, bad pixels or spurious structures are present in one or more of the reduced science frames.
SWarp resamples the input frames, here in the form of FITS images, and projects these onto subsections of the output frames. This projection is done using information given by the input weight maps and in this way creates the final, combined science frame.
The weighted combination, X, for each pixel, j, of N frames with values x and weights w is given by eq. 3.1.

$$X_j = \frac{\sum_{i=1}^{N} x_{ij} \cdot w_{ij}}{\sum_{i=1}^{N} w_{ij}} \tag{3.1}$$

In our case, we have the possibility of including three different factors in the weighted combination of the reduced science frames:

- Noise (flux rms)
- Transparency
- Seeing

Besides the bias- and flat field-corrected science frames, the EsoReflex reduction pipeline, as mentioned earlier, also gives corresponding noise maps to each reduced science frame as an output. These noise maps reflects the flux rms on each pixel in the reduced frame, making it ideal to use as weight when combining the reduced science frames.
The weight term can in this case also be expressed as the relative inverse of the variance (eq. 3.2), and since the variance can be described as the square of the RMS per pixel, σ, the RMS-maps from EsoReflex can be used to directly create weight maps for each reduced science frame:

$$w_i = \frac{1}{{\sigma_i}^2} \tag{3.2}$$

The RMS of the reduced science frames describes the noise of each pixel in the frame. This noise is dominated by the background photons from the sky, but also have contributions from source photons and CCD read-out noise and dark current, the latter connected to the instrument used for obtaining the frames. However, besides looking at the noise contributors, it is also relevant to examine whether atmospheric effects need to be taken into account. This is especially relevant for us, since our data has been obtained with an Earth-based telescope. Furthermore, we are observing at wavelengths in the very blue part of the spectrum, which are particularly affected by atmospheric conditions. Therefore, transparency factors and seeing measurements are included in the configurations for the weighted combination of the reduced science frames.
We compute the transparency by comparing magnitudes of bright stars normalized by the corresponding airmass, as larger airmasses drive to lower quality images. We then use the transparency factors as weights when combining the frames, giving larger weight to frames with higher transparency and, thus, lower airmasses.
Atmospheric seeing is also an important factor to take into account when dealing with atmospheric effects, as this influences the angular resolution of the observations. In our case, we estimate the average seeing to be 0.925 arcseconds. We do so by taking the average of the measured full width at half maximum (FWHM) of the seeing disc, for a number of bright stars in the exposures. We assign larger weights to frames with better (i.e., smaller) seeing.
The final configuration of the weight map used in the combination of the reduced science frames is shown in eq. 3.3. It includes contributions from the flux noise, transparency and seeing, as this was found to be the configuration maximizing the signal-to-noise ratio of the final frame.

$$\sigma_i = \frac{\sigma \cdot Seeing}{Transparency} \ , \ w_i = \frac{1}{{\sigma_i}^2} \tag{3.3}$$

3.3 Alignment of frames

The frames observed with the CFHT u-band filter contain emission in a much larger wavelength-range than the narrow-band filters, as illustrated in Figure 3.1.

In addition, the u-band frames also cover substantially larger areas than the frames obtained with the narrow-band filters.
In order to be able to tie the flux level of the narrow-band frames to that of the u-band frames (see Section 3.5), coordinate alignment is necessary.
By selecting the brightest objects present in both the narrow-band and u-band frames, we pair the coordinates of the objects in common. We then obtain a spatial transformation between these coordinate pairs. By transforming the coordinates of the u-band frame to those of the narrow-band frame, we attain alignment of the frames.
In practice, this is done using the Image Reduction and Analysis Facility (IRAF) software [Tody, 1986], where the tasks *geomap* and *geotran*, specifically developed to obtain and apply spatial transformations on images, are available. We use the AstroPy library [Price-Whelan et al., 2018] in Python to create a list of coordinates for the transformations. We find coordinate pairs for the brightest objects common between the narrow-band and u-band frames. The coordinate list is then passed on to IRAF, from where a spatial transformation between the u-band and narrow-band frames are computed and applied, effectively aligning the frames.
The product of the alignment is an u-band frame with the same reference coordinates as the narrow-band frame. Thus, it is now possible to directly compare the coordinates of sources in both frames. During this whole process, we are altering only the u-band frame, as we wish to retain the information in the reduced narrow-band frame.
Alignment of the u-band frame to the narrow-band frame is a very useful step towards performing photometric calibration of the narrow-band frames. Since the two frames will ideally have the same pixel positions, it will be possible to directly compare the fluxes of common sources in the u-band and narrow-band frames.

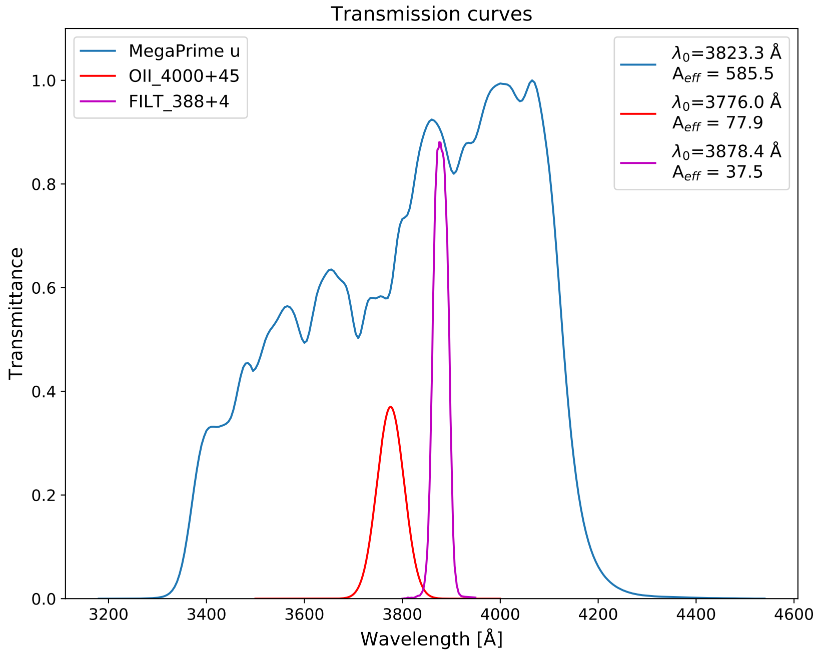

Figure 3.1: Transmission curves of the CFHT MegaCam/MegaPrime u-band filter (blue) and the two VLT/FORS2 narrow-band filters, OII_4000+45 (red) and $FILT$_388+4 (pink), used for the observations of the Strazzullo and Yuan protoclusters.

3.4 Noise Properties

When using a software such as Source Extractor, one of the benefits is that alongside parameter values of extracted sources (e.g., aperture flux values), corresponding errors on these values are also provided.
However, since the extracted fluxes and flux errors are crucial for determining which objects can be classified as Lyα-emitters, we also examine the noise properties of the narrow-band frames in a different manner. We then compare the flux errors from Source Extractor to flux errors estimated by a separate method. By doing so, we will be able to determine whether the noise estimated by this software is suitable to be used when estimating the uncertainties on, e.g., Lyα emission line fluxes.

3.4.1 Background Aperture Photometry

The separate method we use for estimating the noise of the reduced science frames is background aperture photometry.
We use a number of apertures, 100 in this case, and choose their placements to randomly cover the background areas of the science frames. Photometry is then extracted within these background apertures. From here, we obtain distributions of the background aperture fluxes. This allows for comparing these noise estimates

with the aperture flux errors from Source Extractor.
The main reason for doing this double checking of the noise properties is to ensure that we are not introducing noise correlation on aperture scales.
In the case where errors estimated by Source Extractor and background aperture photometry are not consistent, the uncertainties should be scaled in order to make the two noise estimates coherent. This is done by scaling up the noise estimates from Source Extractor, to match the σ of the Gaussian-like flux distribution within apertures placed randomly on the sky.
After going through this comparison, we find that the noise properties from Source Extractor and the background aperture photometry are consistent for the combined narrow-band images of the two protoclusters. This confirms our expectations; besides the reduction and combination of the science frames, no operations has been done on these. Hence the noise should remain the same, regardless of the method used for extracting the photometry.
However, this is not the case for the u-band frames covering each protoclusters. As we describe in Section 3.3, the u-band frames are undergoing spatial transformations, which might introduce some noise correlation. By comparing the noise estimates from background aperture photometry and Source Extractor, we find that for the aligned u-band frames, it is necessary to scale up the uncertainties on fluxes and magnitudes. We find the scaling factors for the Strazzullo and Yuan protoclusters to be 1.46 and 1.59, respectively. Hence, we increase (i.e., multiply) the errors on the flux values and magnitudes by these scaling factors.

3.5 Photometric Calibration

Photometric calibration of observations is fundamental, as it allows for studying the physical properties of the observed objects and for comparing measurements directly to photometric data in public, large catalogs.
Photometric calibration of the narrow-band frames is somewhat difficult in our case though. This is due to the fact that no standard star measurements are currently available for the narrow-band filters used for our observations. However, as also mentioned earlier, CFHT u-band observations covering the protocluster areas are available. Since the u-band frames have already been photometrically calibrated, we can use these frames as a tool to calibrate the narrow-band frames.
This section describes how the fluxes in the narrow-band frame are calibrated to those of the u-band frame, by tying the observed frames together.

3.5.1 Calibrating the Narrow-band Frames

Standardizing the flux measurements for an observation should enforce that the flux densities of bright stars are equal in photometrically calibrated frames. In our case, bright stellar flux densities in the narrow-band frames should be equal to the flux densities of the same stars in the u-band frames from CFHT.
We work under the assumption that the bright stars present in our frames have no absorption or emission lines, so that the fluxes we measure are their continuum

fluxes.
We know that the CFHT u-band is covering the effective wavelengths of the narrow-bands applied (Figure 3.1). Hence, we expect the measured flux density of a star to have the same flux density in the u-band and narrow-band, if the assumption above is valid. In order to calibrate the narrow-band fluxes, we find a factor which describes the relationship between the narrow-band and u-band flux densities. The ratio between the u-band and narrow-band fluxes, for stellar objects only, will function as a calibration factor. We then use this factor to bring the narrow-band fluxes to the same level as the u-band fluxes.
When computing the calibration factor, we ensure that only bright, stellar objects are considered. In order to do so, we apply selection criteria to extracted objects from both the narrow-band and u-band frames. These criteria include restricting the the magnitude of the detected objects, as well as the flux radius. The latter is defined as the radius containing 90% of the light. Eventually, we select stars as bright and compact objects.
The median value of the u-band/narrow-band flux ratio, for the bright stellar sample, is then the factor we apply to the narrow-band, in order to calibrate the photometry of the frames. The calibration factors are found to be 0.876 for the Strazzullo protocluster and 1.299 for the Yuan protocluster.
We know that the calibrated narrow-band flux densities must by definition be equal to the u-band flux densities for objects without any emission or absorption, such as, e.g., stars. When this is the case, the corresponding magnitudes must also be equal. From Figure 3.1 it is evident that both narrow-band filters are close to the central wavelength of the CFHT u-band filter. Hence, we expect the colour, i.e., the difference between magnitudes in two bands (here the u-band and narrow-band), to be centered around 0. Indeed, after applying the calibration factors mentioned above, we find only a small deviation in colour for each protocluster (-0.006 magnitudes for Yuan, 0.008 magnitudes for Strazzullo).

Another correction that might possibly be relevant to take into account is a colour correction of the continuum. We currently assume that any measured narrow-band excess is due to deviations from the continuum, i.e., emission lines. However, if a significant slope in the continuum is present, this can contribute to a measured narrow-band excess originating from the slope of the spectrum itself, and not from a spectral feature. This effect is more relevant when the effective wavelengths of the broad- and narrow-band filters are far apart. Since this is not the case for our observations, we expect this effect to be small for our sample of galaxies. In order to compute an estimate for this, we compare magnitude measurements of objects in the CFHT u-band and the Subaru V-band, in order to examine whether an appreciable slope in the continuum is present in the wavelength range between the u-band and narrow-band filters. We use the same approach as Milvang-Jensen et al. [2013], and find a small colour correction between the u-band and V-band magnitudes, as listed below. As expected, we find that this correction is so small that it will not affect our results.

$$\left(NB-u\right)_{corr}^{Strazzullo} = \left(NB-u\right)^{Strazzullo} - 0.035 \cdot (u-V)$$
$$\left(NB-u\right)_{corr}^{Yuan} = \left(NB-u\right)^{Yuan} - 0.028 \cdot (u-V)$$

Tying Measurements to the COSMOS Photometric Catalog

As mentioned at the very beginning of this section, the photometric calibration of our data is fundamental. By tying the narrow-band observations to u-band observations from CFHT, we have taken a big step towards the calibration of our frames. However, in order to compare our data directly with measurements from the large sky surveys, we need to also tie our frames to these.
We are doing so, by comparing magnitudes extracted with Source Extractor to u-band magnitudes from the COSMOS catalog. We examine the magnitude difference between the two catalogs, also we compute both the median and 3σ-clipped mean of these differences. We find that our measurements are fainter than the measurements from COSMOS by 1.5 magnitudes on average.
This is a substantial, but entirely spurious difference, due to different zeropoints being used to extract the photometric measurements we compared. Therefore, we adjust our zeropoints to match the measurements from the COSMOS catalog.

3.5.2 Extracting Object Catalogs

After the reduced science frames have been photometrically calibrated and tied to the COSMOS catalog, we are now able to extract a catalog of all the sources in the frames covering the Strazzullo and Yuan protoclusters.
We use the Source Extractor software [Bertin & Arnouts, 1996] for this step, using a detection threshold of $1.5\,\sigma$. Hence, we should get a catalog containing photometry of every object with a flux level above 1.5 times the background level of the frames. This catalog will be highly complete, but also contain a large fraction of spurious objects, which we remove by applying further restrictions on the signal-to-noise later on. Source Extractor outputs fluxes, magnitudes, and corresponding errors, within specified apertures. Since we have tied our reduced science frames to the COSMOS catalog, and this catalog has measurements obtained in apertures of $\sim$2 arcseconds, we choose to use an aperture size of 2 arcseconds when extracting photometry from the frames.
We further consider total fluxes and magnitudes for the observed objects. The Source Extractor output parameter *MAG_APER* measures the brightness of an object within a specific aperture, in our case an aperture with a 2 arcsecond diameter. The parameter *MAG_AUTO*, on the other hand, estimates the total brightness of the same object, within a flexible elliptical aperture, defined by the Kron radius. Hence, a conversion factor from aperture to total quantities can be found, by calculating the median difference between *MAG_APER* and *MAG_AUTO*. By using the objects extracted with the zeropoint matched to the COSMOS 2015 catalog (see Section 3.1), we find this factor to be 0.197 and 0.211 magnitudes for the Strazzullo and Yuan protocluster, respectively.
Source Extractor has the possibility of running in dual mode, meaning that it

detects objects in one frame and extracts the photometry of the same objects in another frame. We use this mode for extracting photometry from the narrow-band frames. The u-band frame is used for the detection, as this is deeper and therefore contains a larger number of objects than the narrow-band frames. However, we independently checked that using a combination of the narrow-band and u-band frame as detection image does not affect the final number of reliable Lyα emitters. After extracting photometry on the detected sources, we have obtained two catalogs for each protocluster; a catalog containing u-band photometry and a narrow-band photometry catalog. The u-band and narrow-band catalogs have the same number of entries, as the coordinates used for extracting photometry in both cases are the coordinates of detected u-band sources. Finally, by applying the equations described in Section 2.1, our extraction results in a 5σ Lya limiting flux of 2.18 $\cdot 10^{-17}$ and 5.20 $\cdot 10^{-17}$ erg cm^{-2} s^{-1} within a 2 arcsecond circular aperture for the Strazzullo and Yuan protoclusters, respectively. This limit is mainly set by the depth of the narrow-band follow-up observations, as the u-band observations are much deeper (26.9 AB magnitude in 2" apertures, Muzzin et al. [2013a]).
The extracted photometry is used both when isolating sources with excess narrow-band emission and when computing Lyα emission line and continuum emission for these objects, described in Section 3.6 and 2.1.

3.5.3 Overview of Relevant Galaxy Surveys

Apart from FORS2 narrow-band and CFHT u-band imaging, this thesis also relies on information from some of the large galaxy surveys covering the COSMOS field [Scoville et al., 2007], including the UltraVISTA project, which maps the near-IR section of the spectrum.
COSMOS covers a large area of the sky and therefore has been crucial for obtaining information on galaxies both at high and low redshift. The large redshift-range covered also entails a catalog with galaxies at many evolutionary stages. In the following section, we describe the selection and properties of these surveys.

COSMOS and UltraVISTA

The Cosmic Evolution Survey, COSMOS, is a multi-wavelength survey aimed at investigating the evolution of galaxies [Scoville et al., 2007]. The survey covers a 2 deg^2 field on the sky, centered at:

$$RA: +150.11916667\ (10{:}00{:}28.600),\ DEC: +2.20583333\ (+02{:}12{:}21.00).$$

Using several different instruments, both space- and ground-based, COSMOS has available measurements ranging from X-ray to radio wavelengths. Both of our target protoclusters (see Section 1.2) lie in this field.
The Ultra Deep near-infrared survey carried out with the Visible and Infrared Survey Telescope for Astronomy, UltraVISTA [McCracken et al., 2012], provides photometry for the Y, J, H, and K_s bands.
Ultra deep coverage of 0.73 deg^2 in the COSMOS field is available, consisting of

1408 hours of observations in the four near-infrared bands mentioned above. Deep coverage for the whole UltraVISTA field (1.5 deg^2) is also available for the Y, J, H, and K_s bands, with a total of 212 hours of observations. In particular, we make use of the K_S-band observations to derive an estimate of the stellar mass of the galaxies in our sample (Section 2.3).

3.6 Selection of Lyman-alpha Emitters

Having obtained catalogs of photometrically calibrated narrow-band and u-band sources, we calculate the Lyα emission line fluxes, equivalent widths, and continuum fluxes following the method described in Section 2.1. The initial selection process is made with the purpose of isolating well-detected Lyα emitters. In this thesis, we consider an object as an emitter if the signal-to-noise of the Lyα emission line is ≥ 3. Our initial selection criteria reflects this purpose, but also includes additional limits.
We select only objects with 3σ detection in both the narrow-band and u-band frames. In order to avoid saturated objects, we limit the selection to only include narrow-band magnitudes > 18. Besides these criteria, we impose cuts on the coordinates of the narrow-band frames. We do so in order to avoid false emitter detections due to edge effects, as the background level of the outer edges of the frames is prone to increased scatter.

The most crucial part of the selection process of the Lyα emitters has been the detection of narrow-band excess emission (Section 1.3.2). Galaxies with significant excess emission, compared to the CFHT u-band frame, are clearly distinguishable from non-excess objects on a colour-magnitude diagram, as the ones we show in Figure 3.3. Lines of constant excess are computed using the same definition as Bunker et al. [1995], where larger excess suggest a stronger and, thus, more reliable emitter. This, together with the EW, helps us separate the Lyα emitters from the full sample of extracted objects. In Figure 3.3 we have colour coded the emitters depending on the catalog they are detected in.

By visually inspecting the Lyα emitters, it becomes clear that some of the initially selected emitters are not real objects. These false detections are either caused by edge effects, or problems with background subtraction in the vicinity of bright stars in the narrow-band frames. In order to obtain a sample of reliable Lyα emitters, we cross-match our sample with the COSMOS 2015 catalog [Laigle et al., 2016] and the UltraVISTA K_S- and r-band selected catalogs [Muzzin et al., 2013a]. This allows us not only to match the coordinates of our sample with large survey catalogs, but also provides us with photometric redshifts and photometry in multiple bands for the matched objects.
We check the photometric redshifts from both the COSMOS and UltraVISTA catalogs against the master spectroscopic catalog of the COSMOS survey [M. Salvato, private communication]. Here we find that for low-mass objects at redshifts $\gtrsim 1.8$, the same category we expect our emitters to belong to, photometric redshifts from

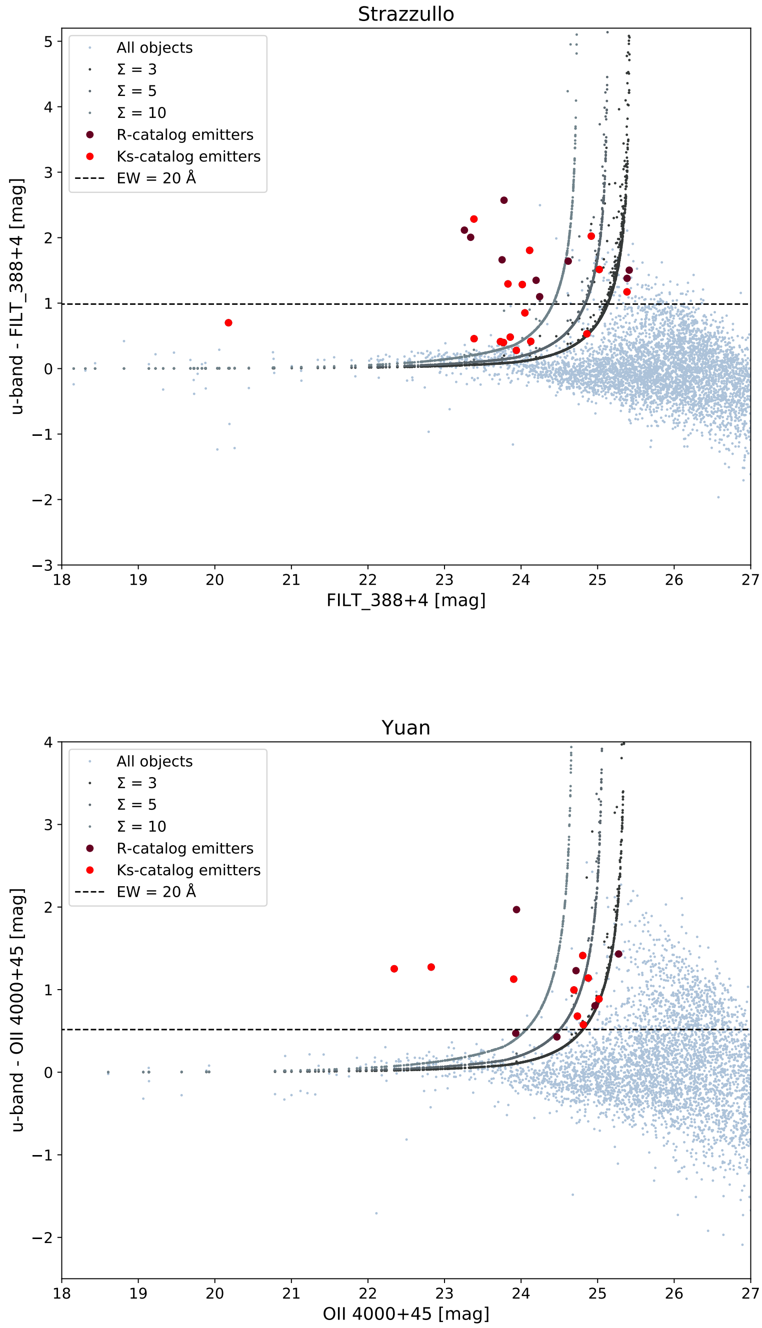

Figure 3.3: Colour-magnitude diagrams of K_S- and r-band selected Lyα emitters in the Strazzullo and Yuan protoclusters. The small, grey symbols show all u-band detected objects in the frames covering the protoclusters, while the larger, red dots show Lyα emitters. Red and maroon symbols show Lyα emitters detected in the UltraVISTA K_S- and r-selected catalogs, respectively. Dotted lines corresponding to a constant excess of $\Sigma = 3, 5$ and 10 are drawn on the diagrams, along with a dashed line showing $EW = 20$Å for reference.

the COSMOS 2015 catalog are more consistent with the spectroscopic redshifts. However, the photometry from the UltraVISTA K_S-band selected catalog is very well tested, which makes it ideal for obtaining the physical parameters for our emitters via SED modeling. Along with the fact that UltraVISTA also has photometry available for sources selected with r-band data, which is closer to our u-band selected data than the K_S-band, we decide to use a combination of the catalogs. We will use photometric redshifts from the COSMOS 2015 catalog and photometry from the UltraVISTA K_S- and r-band selected catalogs.
By using our measurements of the Lyα emission line flux and corresponding flux error, along with the photometric redshifts, we create five quality flags for our sample of Lyα emitters:

- Flag = 0: S/N $\geq$ 5, $\mathrm{z}_{PHOT} \sim \mathrm{z}_{SYS}$
- Flag = 1: 3 $\leq$ S/N $\leq$ 5, $\mathrm{z}_{PHOT} \sim \mathrm{z}_{SYS}$
- Flag = 2: S/N $\geq$ 5, $\mathrm{z}_{PHOT} \neq \mathrm{z}_{SYS}$
- Flag = 3: 3 $\leq$ S/N $\leq$ 5, $\mathrm{z}_{PHOT} \neq \mathrm{z}_{SYS}$
- Flag = 4: Non-reliable objects

Where S/N indicates the signal-to-noise ratio of the Lyα emission line flux, z_{PHOT} is the photometric redshift from the COSMOS 2015 catalog and z_{SYS} is the systemic redshift of the protoclusters (2.19 and 2.095 for the Strazzullo and Yuan protocluster, respectively). The emitters flagged as non-reliable are either objects too close to the narrow-band frame edge or too close to bright stars to be clear detections. By using these flags as additional criteria, we are able to isolate a sample of Lyα emitters, which have secure detections and reasonable redshifts. We decide on using objects with flag 0-2 for the scientific analysis, as we are only interested in well-detected objects and objects with redshifts that are reasonably consistent with the redshifts of the two protoclusters.

After cross-matching our emitters with the COSMOS 2015 and UltraVISTA r-band and K_S-band selected catalogs as well as applying the flags 0-2 described above, we find the following number of Lyα emitters for the two protoclusters: 25 detected in the r-band selected catalog (of which 16 are also detected in the K_S-band catalog) for the Strazzullo protocluster and 15 detected in the r-band selected catalog (of which 9 are also detected in the K_S-band catalog) for the Yuan protocluster.

4 Results and Discussion

In this section we present the final catalog of Lyα emitters as well as number counts, stellar masses and star formation rates. Section 4.1 describes the spatial distribution of our sample of Lyα emitters. In Section 4.2, 4.3 and 4.4, we present our findings on number counts of the Lyα emitters, their colours, and their position on the galactic main sequence. In Section 4.5 we present our final catalog of Lyα emitting protocluster galaxies, while Section 4.6 briefly discusses our findings regarding extended Lyα emission in the Strazzullo and Yuan protoclusters.

4.1 Lyman-alpha Emitters

Having obtained a final catalog of Lyα emitters for both the Strazzullo and Yuan protoclusters, as described in Section 3.6, we are able to compute various physical parameters of these systems. Since we are interested in comparing Lyα emitters within the two protoclusters with Lyα emitters in the field, we choose to investigate if differences are present in physical parameters such as stellar mass and star formation rates. We also examine how the projected number counts of Lyα emitters compares inside and outside of the protocluster environments.

Before going deeper into the stellar mass, star formation rates, and number counts, we start by creating a map of each protocluster, in order to examine how our Lyα emitters are distributed in space. Figures 4.1 and 4.2 show these maps; alongside Lyα emitters, we also show objects with confirmed spectroscopic redshifts. For both protoclusters, the spectroscopically confirmed members are massive, star-forming galaxies with Hα and/or oxygen rest-frame optical emission lines [Kacprzak et al. [2015], Kewley et al. [2016], Valentino et al. [2015], Yuan et al. [2014], V. Strazzullo private communication], while a few additional members are confirmed through Lyα spectra [Lilly et al. [2007], M. Salvato et al. in preparation]. In order to get an idea of the extent of the protocluster structures, we show circles of 500 kpc and 2 Mpc radii. For the Strazzullo protocluster, these are radii from the identified protocluster center, coinciding with the peak of the stellar mass distribution of the candidate cluster members, used to identify this structure [Strazzullo et al., 2015]. However, the Yuan protocluster has several surface density peaks, suggesting that the structure is still merging [Spitler et al., 2012, Yuan et al., 2014]. Therefore, we show circles of 500 kpc radius for each of the surface density peaks originally identified and named by Yuan et al. [2014] and Spitler

et al. [2012], along with a single 2 Mpc radius circle, centered on surface density peak B.
From Figures 4.1 and 4.2 it seems that the Lyα emitters in the Strazzullo protocluster are somewhat filamentary distributed from South to Northwest. However, only a few emitters are present in the immediate surroundings of the central region, where the overdensity of passive galaxies is located. Similarly, only a few Lyα emitters are located near the high-density peaks of the Yuan protocluster, suggesting a possible lack of such objects in the densest regions of both protoclusers.

In order to be able to investigate whether our sample of Lyα emitters are indeed star-forming, low-dust, low-mass objects *and* examine whether their physical parameters are affected by their surroundings, we need more information about these galaxies. In order to get this information, we compute projected number counts as well as total stellar masses and star formation rates of the Lyα emitters, as described in Section 2.

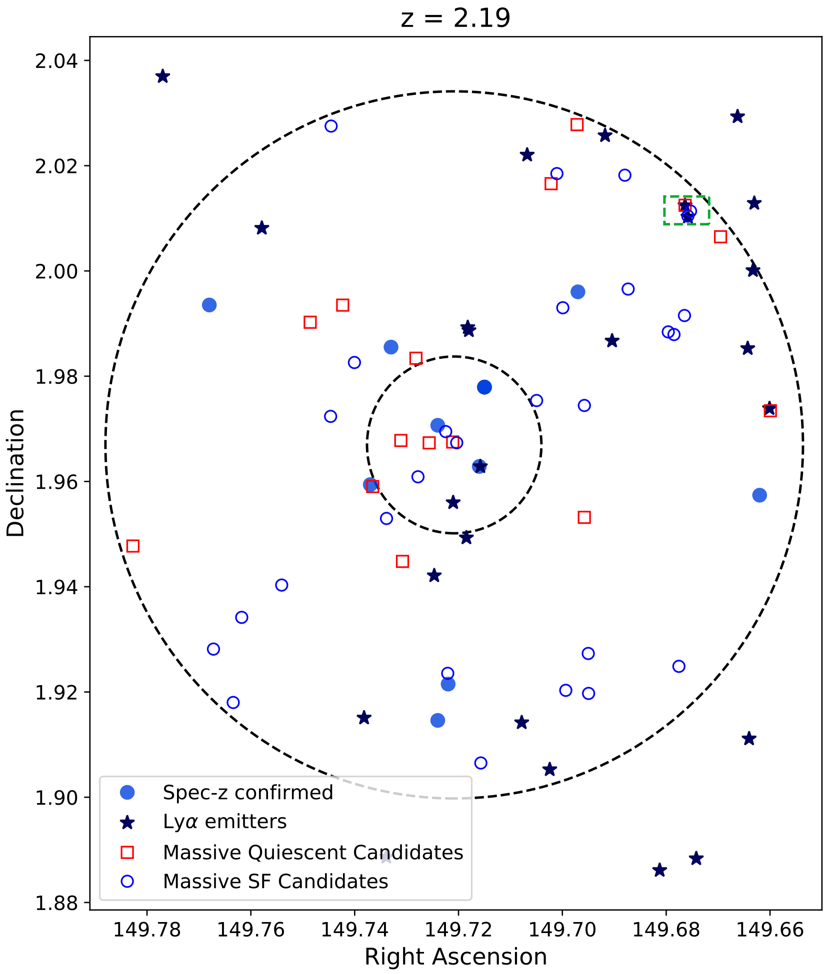

Figure 4.1: Map of the Strazzullo protocluster candidate galaxies. The dashed circles mark radii of 500 kpc and 2 Mpc, respectively, from the adopted protocluster center from Strazzullo et al. [2015]. The green dashed box to the upper right shows the area around an AGN-pair with extended Lyα-emission, covered with the Keck/KCWI spectrograph (see Section 5.2). Dark blue solid stars are the Lyα emitters we detect in this thesis, while blue, solid circles are star-forming objects with confirmed spectroscopic redshifts from the literature (Section 4.1). Open symbols are massive photometric candidates, without spectroscopic confirmation; red squares are classified as quiescent galaxies, while blue circles are classified as star-forming galaxies.

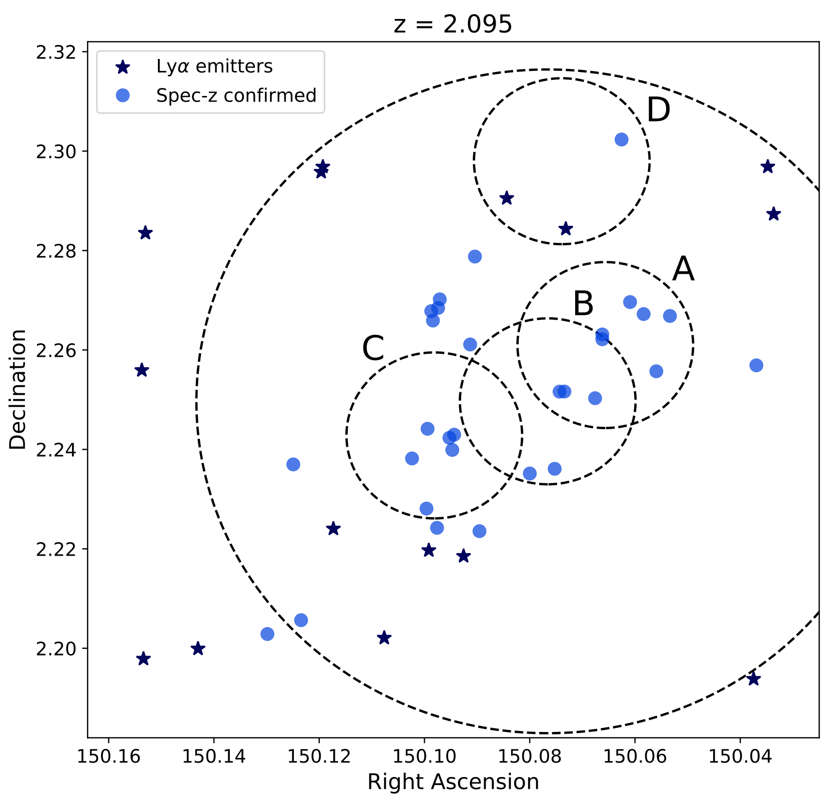

Figure 4.2: Map of the Yuan protocluster candidate galaxies. The smaller, dashed circles mark 500 kpc radii from the center of each overdensity, as defined in Yuan et al. [2014], while the large dashed circle shows a 2 Mpc radii centered on the surface density peak B. Dark blue solid stars are the Lyα emitters we find, while solid, blue circles are star-forming objects with confirmed spectroscopic redshifts from the literature (Section 4.1).

4.2 Projected Number Counts of Lyman-alpha Emitters

One of the main goals of this thesis is to investigate whether the environment surrounding galaxies affects the physical properties of the latter. We are examining Lyα emitters in protocluster regions identified through overdensities of massive galaxies. Such regions should provide ideal conditions for investigating environmental effects. However, we also want to examine whether it might be possible to trace such protocluster regions using Lyα emission. Therefore, we compute projected number counts of our sample of Lyα emitters, and compare these to expected values for the general field.

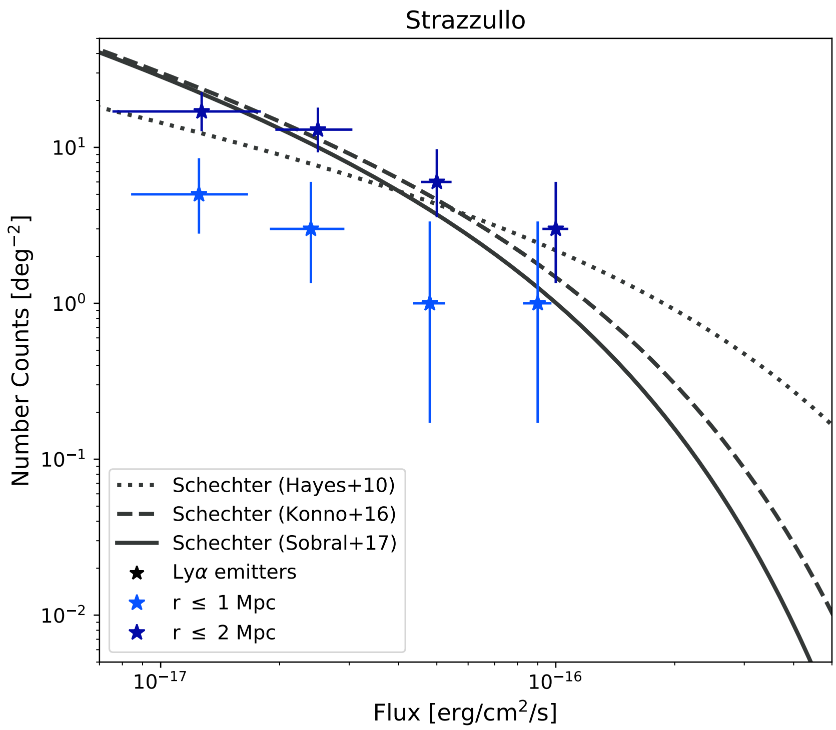

Figure 4.3: Number counts of Lyα emitters in the Strazzullo protocluster. Solid, dashed, and dotted lines show the count estimates derived by integrating the Schechter luminosity functions for Lyα, presented by Sobral et al. [2017], Konno et al. [2016], and Hayes et al. [2010]. Dark and light blue symbols show number counts of Lyα emitters within 2 Mpc and 1 Mpc radii from the protocluster center, respectively. Within a radius of 1 Mpc, we find the number counts of Lyα emitters to be lower than the expected values for the field.

For each protocluster, we compute number counts of Lyα emitters within circular areas of 1 Mpc and 2 Mpc radii. These radii are measured from the central coordinates of the Strazzullo protocluster, while for the Yuan protocluster, we compute number counts within areas centered on the four identified surface density peaks. We note that the resulting number counts are limited by the depth of our observations and, thus, we are only able to draw conclusions for objects with Lyα

emission above the limiting flux of our observations.
We compare our results with number counts derived from three different Lyα luminosity functions, all computed for redshifts of $\sim$2.2, presented by Hayes et al. [2010], Konno et al. [2016], and Sobral et al. [2017]. These values are derived by integrating a Schechter function over redshift in order to obtain the number density of galaxies. We then multiply the number density from this integration, and the number density of our sample of Lyα emitters, with circular areas of radius 1 Mpc and 2 Mpc, which results in the number counts of galaxies within these areas of the protoclusters. We show the resulting number counts of our sample, as well as the estimates from the three Lyα luminosity functions, in Figures 4.3 and 4.4. Errors on the number counts are computed from Poissonian statistics and represent 68% confidence intervals, while we use bootstrapping in order to constrain the errors on the fluxes.

4.2.1 Comparison with Field Number Counts

In order to investigate whether our sample of Lyα emitters are affected by the protocluster environments, we compare the number counts of these emitters with expected values for the general field of galaxies. We find that within a 2 Mpc radius, the number counts of Lyα emitters fits reasonably well with the values derived from the luminosity functions, especially the one presented by Hayes et al. [2010]. Since these luminosity functions should be representative for the general field of Lyα emitters, our result suggests that the Lyα emitting protocluster galaxies are contained within a radius smaller than 2 Mpc. This even seems to be the case for the Yuan protocluster, though there is evidence of several surface density peaks in this structure, indicating that the protocluster is still merging. Hence, we find no indications of either of the protoclusters extending way larger than 2 Mpc down to our Lyα limiting depth.
While we do not see any great variations from the field expectations for number counts of Lyα emitters within 2 Mpc radii, our results do suggest a different story on smaller scales. Within 1 Mpc radii, we find that the number counts of Lyα emitters are *below* the expected values for both the Strazzullo and Yuan protoclusters. This not only indicates that the effect of clustering is more prominent within 1 Mpc from their center, but also that these structures might be affecting the enclosed galaxies. As mentioned earlier, we use Lyα emission as tracer of star formation and, thus, we assume that our sample of detected Lyα emitters are dominated in number by star-forming galaxies. The fact that we find a lack of Lyα emitters within both protoclusters suggests that something is inhibiting star formation in these protocluster galaxies, possibly leading to quenching of the latter in the near future.
For the Yuan protocluster, we observe that the number of Lyα emitters differ between the four different surface density peaks. From the data currently available for this protocluster, as also presented in Figure 4.4, we find that surface density peak D has the most Lyα emitters, while surface density peak B is completely

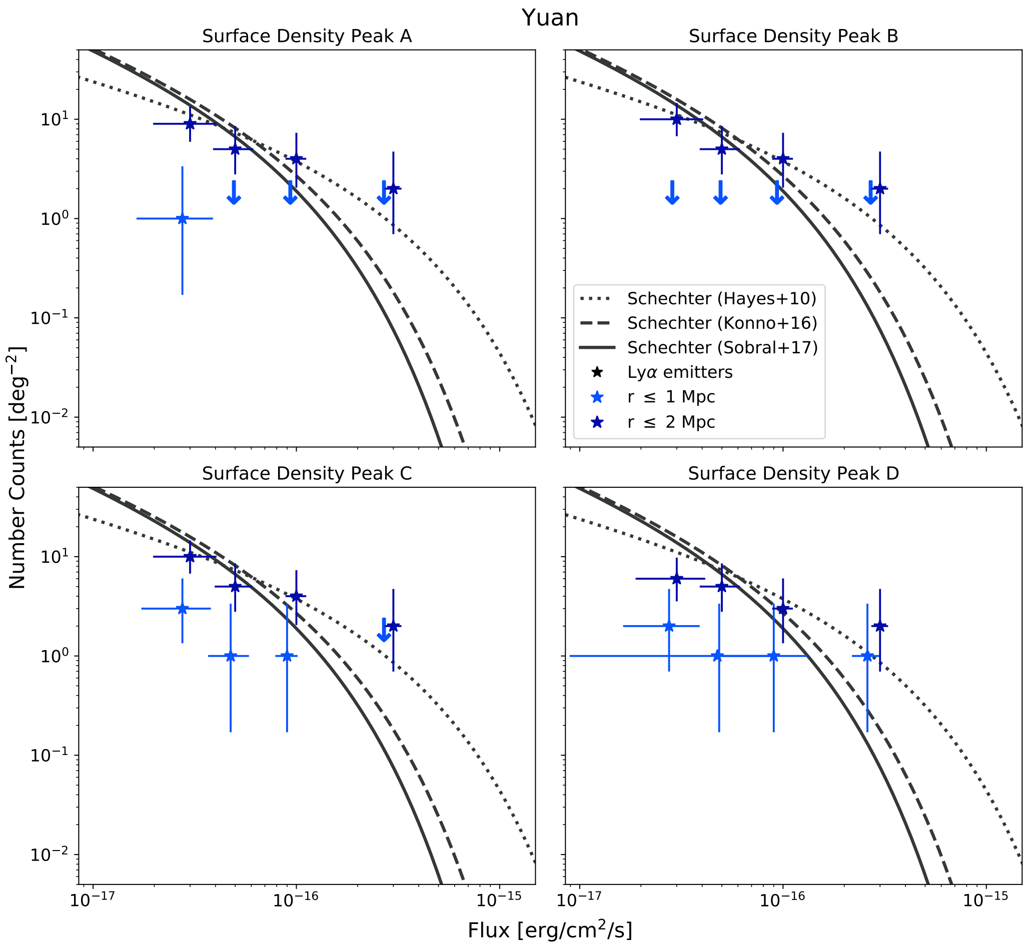

Figure 4.4: Number counts of Lyα emitters in each of the four surface density peaks of the Yuan protocluster. Solid, dashed, and dotted show count estimates derived by integrating the Schechter luminosity functions for Lyα, presented by Sobral et al. [2017], Konno et al. [2016], and Hayes et al. [2010]. Dark and light blue symbols show number counts of Lyα emitters within 2 Mpc and 1 Mpc radii, respectively, from the centers of the surface density peaks. Arrows show 3σ upper limits on the number counts in cases where no Lyα emitters are detected within the chosen radii.

cleared of such. The number counts presented in Figures 4.3 and 4.4 are computed for 3σ detected fluxes, meaning that we are confident that these quantities are representative for our sample of Lyα emitters. However, we cannot be completely sure how this trend evolves for fluxes below the 3σ flux limit (see Section 3.5.1). Two possible alternative trends might occur at fluxes below our threshold depth; either the number counts of Lyα emitters in the protoclusters are steadily lower than in the field, or they increase and might possibly overshoot the expectations for the general field. In the first case, we would naturally interpret the lack of faint Lyα emitters to be due to stronger quenching. This scenario would be plausible, as low-mass galaxies are expected to be more affected by the protocluster halo (see Section 1.2.2). Therefore, if the protocluster environment causes quenching of the enclosed galaxies, this trend should be even stronger for low-mass objects. If this is the case, deeper observations should result in a drop in the number counts of Lyα emitters at lower flux levels. This would only cause the number counts of such objects to diverge even further from the values for the general field. An enhancement of Lyα emitters at lower flux levels would thus be puzzling, if what we observe is indeed correct.

Hence, deeper observations would make it possible to constrain the number counts of Lyα emitters at lower flux levels and, thus, make us able to test our hypothesis that we are observing environmental quenching already at $z \geq 2$. Currently, we are also limited by low number statistics, which impose some difficulties in drawing general conclusions from our sample of Lyα emitting galaxies. Sobral et al. [2017] finds that for Lyα luminosities above $\approx 10^{43}$ erg s^{-1}, the number counts of Lyα emitters in the general field are best described by a power-law. While we find that this could be the case, especially for the Yuan protocluster, our sample is simply not large enough to conclude whether this is also the case for Lyα emitters located within protocluster environments.

When examining number counts, especially within a relatively small area on the sky, it is also relevant to consider whether cosmic variance could affect our results. Cosmic variance reflects the fact that observations of different parts of the sky might differ from each other, due to the large scale structure of the Universe. Even though we are looking for variances, due to the presence of protocluster halos, cosmic variance could affect our measurements, as the Strazzullo and Yuan protoclusters are located at different positions on the sky. However, we observe the same trend in both protoclusters, at similar redshifts, and we also find that on larger scales, the number counts of Lyα emitters approach values expected for the general field. While it could be interesting to examine the effect of cosmic variance on our sample in more detail, our results suggest that we are observing physical effects of the protocluster environment on Lyα emitting galaxies.

It should also be noted that starting from luminosity functions is only one method for comparing number counts of the protocluster galaxies with expectations of projected number counts for the general field. Another method that might also be relevant to apply is nearest neighbour algorithms (see Strazzullo et al. [2015] for the application to the photometric candidates of their clusters). These algorithms work by measuring the average distance between galaxies in the field and compare this to the average distance between galaxies within a specific area, e.g., a protocluster. We think it would be interesting to apply this approach on our sample of Lyα emitters as well, to examine if it supports the same trend as the luminosity functions: that there is a deficit of Lyα emitters within the Strazzullo and Yuan protoclusters.

4.3 Rest-frame UVJ Colours of Lyman-alpha Emitters

As mentioned in Section 1, we expect Lyα emitters to be mainly star-forming galaxies with low dust content and low stellar masses. Hence, we expect the emitters from our catalog to show blue colours and, thus, to be located in the lower and left region of a restframe UVJ-diagram [Williams et al., 2009, Wuyts et al., 2007]. This and similar colour-colour diagrams (e.g., the BzK-diagrams mentioned in Section 1.2.4 [Daddi et al., 2004]) are powerful tools to separate blue star-forming galaxies from red quiescent objects, mapping the region around the prominent Balmer break. By creating such a colour-colour diagram, see Figure 4.6, we observe that the majority of our sample of Lyα emitters are indeed located in the lower left region, corresponding to the emitters being classified as star-forming galaxies. However, the emitters are not located within a confined area of the UVJ-diagram; some are located slightly towards the more red objects, while others are borderline to being classified as quiescent. This indicates that our catalog of Lyα emitters is not as uniform as first expected. Notice that we show only emitters detected in the K_S-band, as no near-IR emission is detected for emitters detected only in the r-band.

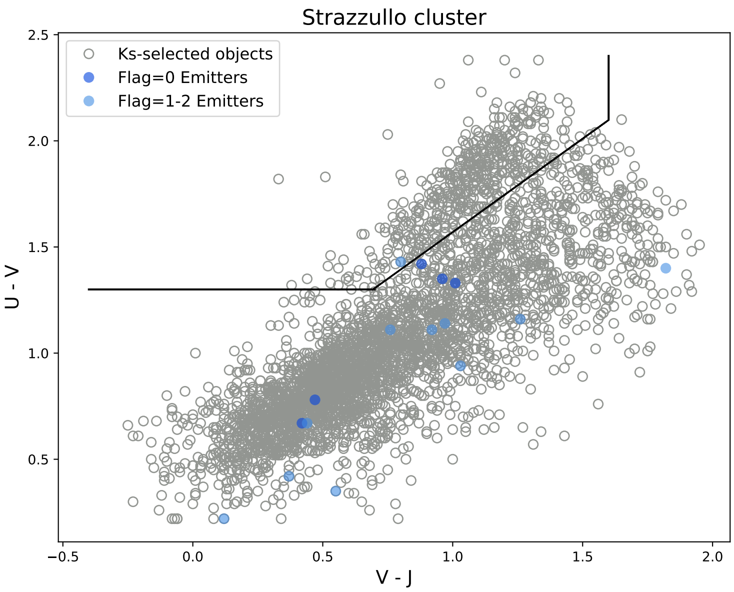

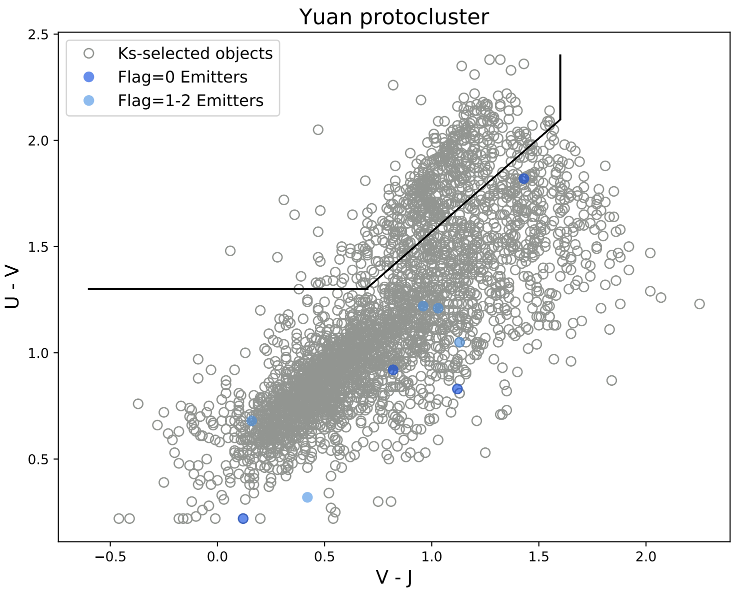

Figure 4.6: Rest-frame UVJ colour-colour diagrams of K_S-band detected emitters. Grey symbols show all K_S-band detected objects in the u-band frame covering the same region as the narrow-band frames. Blue symbols show Lyα emitters. Light blue symbols show detected Lyα emitters with quality flags 1 and 2, while darker blue symbols show Lyα emitters with quality flag 0. Flags are described in Section 3.6. Black, solid lines are drawn in order to separate star-forming and quiescent galaxies, using the box regions described by Muzzin et al. [2013b] $(U - V > (V - J) \cdot 0.88 + 0.69)$. Emitters detected in the r-band only cannot be shown here, as they do not have significant emission in the near-IR.

4.4 Main Sequence of Lyman-alpha Emitters

Counting Lyα emitters within and outside the two protocluster regions suggests that an early quenching of the brightest emitters might occur within these structures. In this section we test this suggestion by comparing SFRs of individual protocluster emitters with the general expectations for field galaxies at fixed stellar mass. For the latter, we use the main sequence defined by Sargent et al. [2014] as reference. We compute the main sequence at the redshifts of both the Strazzullo and Yuan protoclusters and find that there is only a very small difference between the relations at each redshift. Due to this minor difference, and in order to simplify the visual representation, we choose to only use a single main sequence relation for the comparison, computed for z = 2.19.

When examining the distribution of Lyα emitters on the main sequence, we use two approaches: we first distinguish between the Lyα emitters found in each protocluster, then we consider all the emitters together, regardless of their host protocluster, and instead distinguish between the extinction of these Lyα emitters. We use the first approach to inspect whether one of the protoclusters stands out in terms of M_* and/or SFR of the Lyα emitters. The second approach is for examining how the extinction of the Lyα emitters are distributed over the main sequence.

Uncertainties on M_* are determined from χ^2 minimization (68% confidence limits) during the SED-fitting, the upper limits on M_* are at 3σ. Uncertainties on the SFRs are determined through standard error propagation, where we show the errors on the fluxes, but not on the dust correction. Both of these parameters are described in further detail below.

4.4.1 Star Formation Rates

In this thesis we make use of three different star formation rate estimates. We use SFRs obtained through SED-fitting using constant star formation history, as well as star formation rates estimated from UV- and Lyα-luminosity (see Section 2).

The SFRs from both UV- and Lyα-luminosity represent dust-corrected values. We apply dust correction directly to the UV-luminosity, which we then use when estimating SFR_{UV}. However, while $\mathrm{SFR}_{Ly\alpha}$ also predicts the intrinsic SFR, we compute this quantity using the observed Lyα-luminosity. Even though Lyα emission is a powerful tracer of star-formation, using the observed luminosity as tracer of SFR might prove problematic for Lyα emitting galaxies with high dust content. Indeed, $\mathrm{SFR}_{Ly\alpha}$ deviates the most from SFR_{UV} in cases where $A_V \gtrsim 0.5$, as evident from Figure 4.10 and Tables 4.1 and 4.2. Thus, the calibration of $\mathrm{SFR}_{Ly\alpha}$ seem to fail for very dusty objects.

We use a well established method for estimating SFR from UV-luminosity and we find that SFR_{UV} is coherent with $\mathrm{SFR}_{Ly\alpha}$ for objects with low dust content, consistent with the $\log_{10}\left(\mathrm{SFR_{Ly\alpha}}/\mathrm{SFR_{UV}}\right) = 0.23 \pm 0.24$ reported in Sobral & Matthee [2019]. On the other hand, we derive fully consistent SFRs from SED fitting and UV-luminosity. In the following analysis, we will make use of SFR_{UV}, however the results does not change if we adopt the SED-based estimates. We reach similar conclusions for galaxies with low dust content by correcting $SFR_{Ly\alpha}$ by the factor ∼0.23 dex, also mentioned above, while we derive more uncertain results for objects with higher dust content ($A_V > 0.5-1$ magnitudes).

4.4.2 Stellar Masses

We estimate stellar masses both by converting K_S-luminosities and by modeling the full SED, as described in Section 2.3. In both cases, in order for the stellar masses to be reliable, a detection (i.e., S/N≥3) in the K_S-band is crucial. However, we find that only about 2/3 of our sample are available in the UltraVISTA K_S-band selected catalog. Hence, SED-fitting will only produce meaningful values of M_* for the K_S-brightest, and therefore most massive, among our Lyα emitters. The emitters detected in the r-band selected catalog do not have detections in the near-IR bands, and therefore have partly unconstrained SEDs.
We go through two different approaches for estimating M_* of the galaxies not detected in the UltraVISTA K_S-band selected catalog. We rescale the SEDs of galaxies with detections in the K_S-band to the SEDs of galaxies not detected in the K_S band, and also use mass-to-light ratios to compute upper limits on the M_* (see Section 2.3). Both approaches are described in the following sections.

M_* from SED-extrapolation

We use photometry from the UltraVISTA K_S- and r-band selected catalogs to inspect the SEDs of our Lyα emitters. The Lyα emitters detected only in the r-band selected catalog are all unconstrained in at least one of the near-IR bands: K_S. We attempt to estimate M_* of these objects by rescaling the SEDs of K_S-band detected objects to the r-band flux of the non-K_S detected SEDs.
We start out by sorting the K_S-detected SEDs into two groups, based on the criteria we use on the U-V, and V-J colours (see Figure 4.6). We then take the median of the SEDs in each group, in order to avoid outliers. These averaged SEDs, shown in Figure 4.7, are then used as templates for the extrapolation. However, when rescaling the template SEDs to the r-band flux of the non-K_S detected SEDs, it quickly becomes clear that the latter have much steeper slopes than both of our median templates, as the non-K_S detected emitters have rapidly decreasing flux densities towards the red part of their SEDs. Because of this, we choose to use only the bluest of the K_S-detected SEDs, for each cluster, as template instead. We use the same method as before; rescaling this new template SED to the r-band of the non-K_S detected SEDs. As Figure 4.8 shows, the template SED does not match the slope of the bluest emitters among the non-K_S detected ones. As also evident from Figure 4.8, we should be able to detect this object, if its SED were similar in shape to that of the template SED. Since the objects are indeed not detected, we conclude that none of the template SEDs we explored are able to properly describe all the non-K_S detected Lyα emitters. Therefore, if we were to estimate M_* by rescaling the template galaxy's SED-fitting, then this would result in a considerable over-estimation of M_* for the non-K_S detected galaxies. Though Figure 4.8 is only showing a single example of the attempted SED-extrapolation,

we find that this is a common trend for most of the Lyα emitters not detected in the K_S-band. SEDs of all the non-K_S detected emitters are shown in Appendix A. Hence, we find that this method is not a good choice for constraining the M_* of these galaxies.

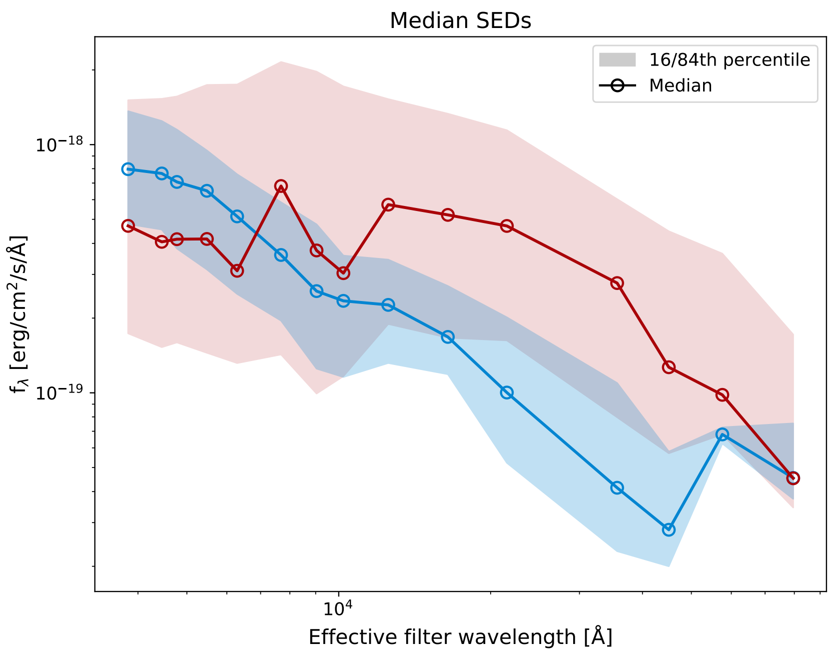

Figure 4.7: Templates used for extrapolation of the SEDs of Lyα emitters not detected in the K_S-band. These templates are created by first grouping the SEDs of objects *with* detection in the K_S-band, based on their location in the UVJ-diagram (Figure 4.6). This results in two sets of SEDs; one with SEDs of objects classified as red and another with SEDs for objects classified as blue, based on their UVJ-colours. By taking the median of the SEDs in each group, we create the template SEDs shown on this figure. Contours around the SED templates show the corresponding 16^{th} and 84^{th} percentiles for each template.

M_* from Mass-to-Light Ratio

Before using the mass-to-light ratio (see Section 2.3) to estimate M_* of our sample of non-K_S detected Lyα emitters, we calculate M_* for objects that *are* detected in the K_S-band. Since we already know M_* for these objects through SED-fitting, we can use these to test the mass estimation from the mass-to-light ratio. We find a clear correlation between M_* from SED-fitting and M_* computed using the mass-to-light ratio, however, a slight offset is present between the two. We compute the median of this offset and find that M_* from the mass-to-light ratio, $M_*^{M/L}$, needs to be corrected by a factor of 0.32 dex, in order to be consistent with the M_* from SED-fitting.

Taking this correction into account, we use the mass-to-light relation to compute

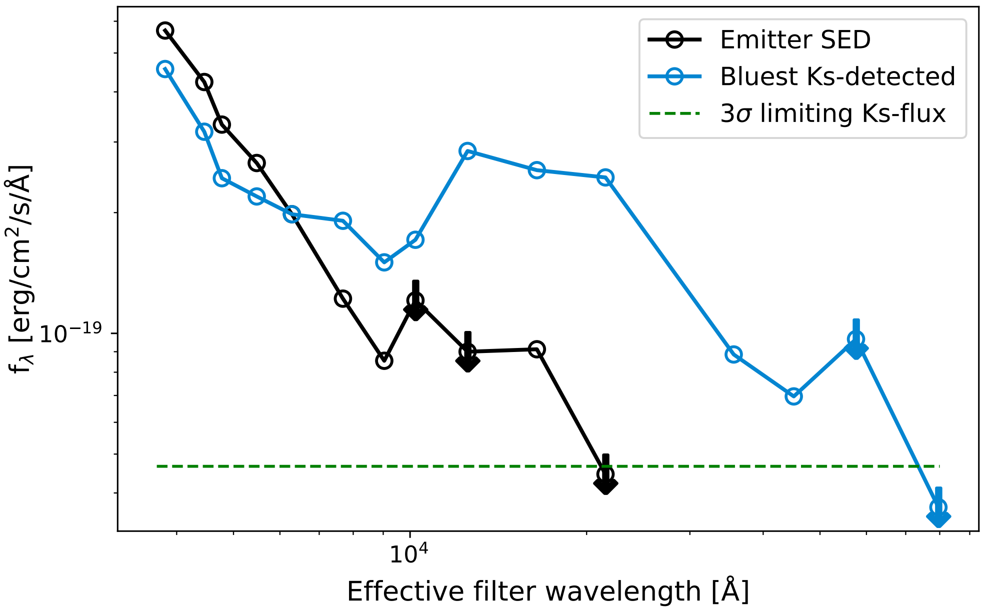

Figure 4.8: Example of K_S-band detected SED rescaled to a SED not detected in the K_S-band. The blue SED shows the bluest of the K_S-band detected galaxy SEDs. We rescale this SED to the r-band of the SED with no detection in the K_S-band, shown in black. We do so, since we are sure that these objects are all detected in the r-band, as we locate them in the UltraVISTA r-band selected catalog. The green dashed line show the 3σ limit on the K_S-band flux density.

$M_*^{M/L}$ for the Lyα emitters not detected in the K_S-band. We adopt the 3σ upper limit on the K_S-band flux to compute the total K_S-luminosity, which is needed for the calculation of $M_*^{M/L}$. Hence, it should be noted that the computed values of $M_*^{M/L}$ are in this case only upper limits.

4.4.3 Comparison with Expected Main Sequence

When comparing M_* and SFRs of our sample of Lyα emitters to the general main sequence of galaxies from Sargent et al. [2014], we find that the two are not entirely consistent. As we show in Figure 4.9, our sample of Lyα emitters are not homogeneous. We find that the emitters, in both the Strazzullo and Yuan protocluster, span a wide range of both M_* and SFR, which is contrasting with our first expectations. Lyα emitters are often associated with being low-mass, star-forming galaxies with relatively low dust content. While part of our sample might indeed be classified as low-mass galaxies, we also detect emitters with stellar masses of the same order as what is expected for more evolved galaxies. The star formation rates of our sample galaxies also differ quite widely, ranging from less than one to several thousand solar masses per year.
The dust content of the Lyα emitters does not appear directly from the main sequence. Therefore, we assign colours to our sample depending on their dust

extinction, which is found through SED-fitting. We do so, in order to investigate how galaxies with high- and low dust content are distributed on the main sequence. The A_V-colour coded main sequence is presented in the right panel of Figure 4.9.

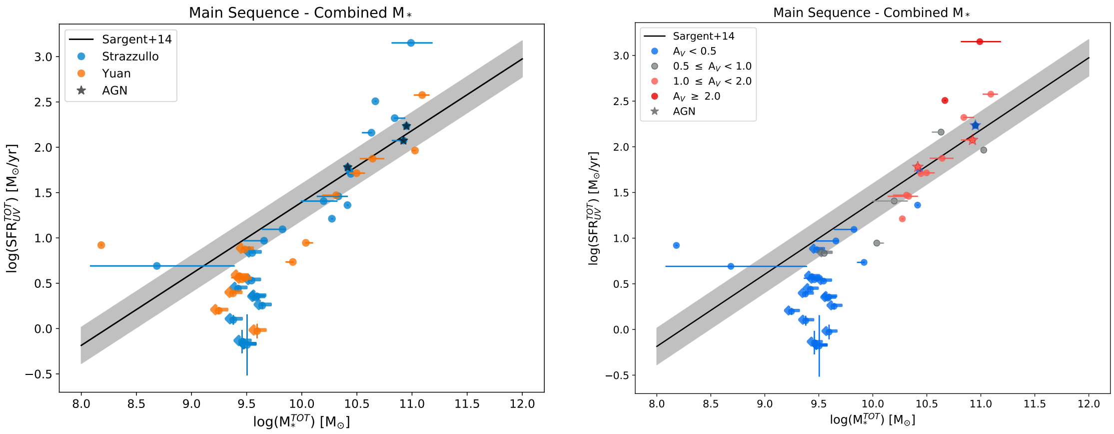

Figure 4.9: Stellar mass vs. star formation rates, or the galactic main sequence, for the Lyα emitters in both the Strazzullo and Yuan protocluster. The black line shows the main sequence presented by Sargent et al. [2014], with contours showing typical scatter of ± 0.2 dex. The left panel shows how the Lyα emitters in the Strazzullo (blue) and Yuan (orange) protoclusters are positioned with respect to the main sequence. The right panel shows Lyα emitters on the main sequence, colour coded by their dust extinction, A_V. Blue and grey colours indicate $A_V \leq 1.0$ magnitudes, while red colours indicate $A_V \geq 1.0$ magnitudes. Stars show confirmed AGN, all located within the Strazzullo protocluster. Arrows show 3σ upper limits on the stellar mass.

By colour coding our sample of Lyα emitters based on their extinction, we find that it somewhat matches our expectations. Galaxies with the lowest M_* seem to also be the least dusty objects. For objects with larger M_* and SFR, we expect higher dust content due to enrichment from stellar feedback, which is consistent with what we find.

In general, we find that the SFR of our sample, for a fixed value of M_*, is lower than expected for main sequence galaxies in the field. Hence, the majority of the Lyα emitters in our sample are located *below* the main sequence of galaxies. This suggests that the Lyα emitters within the Strazzullo and Yuan protocluster are less star-forming, compared to field galaxies with same stellar mass. Though it is difficult to determine if this lack of star formation is linked to environmental effects of the protocluster halos, it could be an indication that the Lyα emitters are in the process of being quenched. This is consistent with the results presented in Section 4.2; our findings on the number counts of Lyα emitters support the idea of quenching, as we not only find Lyα emitters with lower SFRs than expected, but also less Lyα emitters than what is expected, with respect to the field.
However, quenching is not the only possible explanation for the Lyα emitters having lower SFRs than predicted by the galactic main sequence. Some of these

emitters might currently not be very active in forming stars, not necessarily meaning that they are becoming quiescent. Since we are using Lyα- and UV-emission as tracer of star formation, we are only able to measure instantaneous star formation. Hence, we cannot draw conclusions on how the star formation in these galaxies are going to change over longer timescales.
On the other hand, we also find a few Lyα emitters which have SFRs higher than what is predicted for their stellar mass. Even though these galaxies are consistent with our expectations that Lyα emitters are star-forming, some of them are neither low-dust nor low-mass objects. Especially two of these objects are interesting. We observe a galaxy of low stellar mass ($\sim 10^8 M_\odot$), which is detected in the K_S-band and have SFR significantly above what is predicted from the main sequence. We also observe a high-mass ($\sim 10^{11} M_\odot$) Lyα emitting galaxy, which has high dust content and SFR well above the predicted value. We can generally classify these objects as 'starbursts', but, given their widely differing stellar masses, they likely represent two different categories of objects, possibly driven by different mechanisms. While blue, starbursting Lyα emitters with low stellar masses are somewhat common, since a minimal amount of gas and a low dust content are enough to trigger Lyα emission from star formation, the massive object is more puzzling and its large dust extinction makes us cautious against the reliability of the estimate of its SFR. The nature of these two objects would be interesting to examine further, e.g., through planned spectroscopic observations (see Section 5).
Another interesting feature of the main sequence of our sample of Lyα emitters, is the fact that there seem to be a lack of emitters around $\mathrm{M}_* \sim 10^{10} M_\odot$ on the main sequence. Though it is difficult to establish if this feature is significant from our sample alone, e.g., due to the observation depth and low number statistics, we should be able to detect Lyα emitting galaxies with a stellar mass of $10^{10} M_\odot$. However, it could be that star-forming galaxies in this mass-range are indeed present in the protoclusters, but that they have too high dust content to be detected in our narrow-band frame. Though we do not expect this to be the case, as we detect Lyα emitters with large values of A_V at $\mathrm{M}_* > 10^{10}$ $\mathrm{M}_\odot$, this could still be one of several possible selection effects for our data. We will describe some of these in further detail below.

Possible Selection Effects

When obtaining a sample, in this case of galaxies with significant Lyα emission, there is always a possibility that this sample is influenced by various selection effects. In our case, we know that we are limited by the depth of our observations and, thus, we detect only objects above a certain flux level. We expect the objects that are too faint to be detected to be of even lower mass than our current sample. However, we cannot be sure that these are the only objects that we are not able to detect. We know that the amount of Lyα emission we receive from a galaxy is highly dependent on the escape fraction of Lyα photons. This escape fraction is affected by the morphology of the emitting galaxy. Large amounts of neutral gas and dust around Lyα emitting regions can cause the emitted photons to be absorbed or scattered, thus making them impossible to detect. This is especially troublesome if the interstellar medium of a galaxy tends to be clumped or anisotropic. Though it is more realistic to assume that the ISM of a galaxy is clumpy, the Lyα escape fraction becomes more difficult to predict, as it might then vary through different parts of the galaxy, causing Lyα photons to be more likely to escape in some regions than others. Outflows and accretion can also affect the radiative transfer of the Lyα photons, which can cause difficulties when observing Lyα emission from, e.g., AGN host galaxies. This also suggests that we might not be able to detect galaxies with ongoing star formation, if these galaxies are obscured by dust, as most of the Lyα emission will not escape such a galaxy. Combined measurements, using, e.g., UV and IR filters, could help avoid some of these selection effects, as emission at these wavelengths can also be used as tracer of star formation.

4.4.4 Comments on Stellar Mass and Star Formation Rate

Since we rely on the concept of the main sequence of galaxies to compare our sample of Lyα emitters with field galaxies, we add some comments about the two parameters involved in such relation, namely the SFR and stellar mass.
As mentioned in Section 4.4.2, we use stellar mass estimates from SED-fitting for Lyα emitters detected in the UltraVISTA K_S-band selected catalog. For objects not detected in the K_S-band, we use the mass-to-light ratio described by Arnouts et al. [2007] to obtain upper limits on M_*. These upper limits are used solely for the purpose of placing objects not detected in the K_S-band on the main sequence. Thus, we are not able to draw firm conclusions based on these stellar masses, as the upper limit is the only constraint that we have on these. We can say that these are low-mass galaxies, but we are not able to determine their exact mass, which is why we do not know if these Lyα emitters are located above, below, or are consistent with the predicted main sequence from Sargent et al. [2014].
As for the star formation rates, we find a discrepancy between the SFRs computed using UV-luminosity (or, equivalently, the SED modeling) and those computed using Lyα luminosity and rest-frame equivalent width of the Lyα emission lines. Sobral & Matthee [2019] report an over-prediction of factor 0.23$\pm$0.24 dex between SFR$_{Ly\alpha}$ and SFR$_{UV}$. However, we find a discrepancy between the two which cannot be explained solely by this over-prediction. Even though both SFRs should describe dust corrected quantities, the difference between SFR$_{UV}$ and SFR$_{Ly\alpha}$ seem to have a dependency on extinction. By examining this discrepancy's dependence on A$_V$, which we show in Figure 4.10, we find that the largest differences between SFR$_{UV}$ and SFR$_{Ly\alpha}$ occur for the most dusty objects. This might explain why we see such large differences between the two SFR estimates, as SFR$_{UV}$ are estimated using dust corrected luminosities, while SFR$_{Ly\alpha}$ should predict dust corrected SFRs, but are estimated from the observed Lyα luminosity. Due to this difference between the estimated SFRs, we choose to use the SFR estimates from dust corrected UV-luminosity when representing the main sequence, as this relation is the most well established of the two.

Finally, we note that the SFRs computed for the three confirmed AGN in the Strazzullo cluster (marked with stars on Figure 4.9 and 4.10) might not represent the true SFR of these galaxies. Even though these emitters seem consistent with the main sequence, the UV and Lyα emission from these galaxies cannot be assumed to origin from star formation only. Accretion onto the central black hole of these galaxies produce extremely high luminosities with emission at almost all wavelengths. Thus, part of the detected Lyα emission from these galaxies is likely not to originate from star formation, but from photoionization of the surrounding medium, caused by the active galactic nucleus. However, this is not taken into account when computing the star formation rates, which is why one should be cautious about the SFR of these three sources.

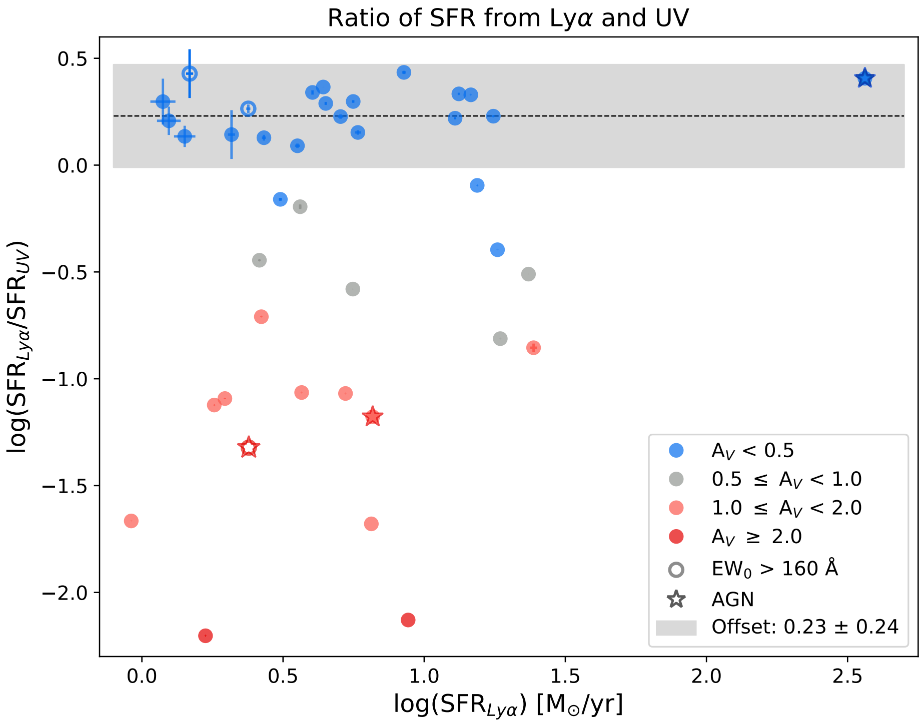

Figure 4.10: Ratio of star formation rates estimated from Lyα and UV luminosities, colour coded by A_V. The black dashed line and grey contours show the offset and corresponding scatter (0.23±0.24 dex) between SFR_{UV} and $SFR_{Ly\alpha}$ predicted by Sobral & Matthee [2019]. Blue symbols indicate extinction values, A_V, below 0.5 magnitudes. Grey symbols show emitters with $0.5 \leq A_V < 1.0$ magnitudes. Coral symbols show emitters with $1.0 \leq A_V < 2.0$ magnitudes. Red symbols show emitters with $A_V \geq 2.0$ magnitudes. Open circles represent Lyα emitters with rest-frame equivalent widths above 160 Å. Stars show the three AGN located within the Strazzullo protocluster.

4.5 Final Emitter Catalog

The final catalog of Lyα emitters contains the stellar masses and star formation rates described above. Furthermore, it also contains extracted information about dust extinction and photometric redshifts, when available. In Tables 4.1 and 4.2 we present these parameters for our whole sample of Lyα emitters. In addition, we also show the emitter ID from the UltraVISTA catalog, as well as the quality flag of the emitters (see Section 3.6), and in which catalog (UltraVISTA K_S- or r-band selected) they are detected.

This final catalog provides us with all the information we need, in order to compare number counts of the Lyα emitters within and outside the Strazzullo and Yuan protoclusters, as well as to place these emitters on the main sequence of galaxies.

Table 4.1: Strazzullo Protocluster

ID	M_*^{TOT} [log(M$_\odot$)]	SFR$_{CSF}$ [log(M$_\odot$/yr)]	SFR$_{UV}^{TOT}$ [log(M$_\odot$/yr)]	SFR$_{Ly\alpha}^{TOT}$ [log(M$_\odot$/yr)]	A$_V$ [mag]	z$_{PHOT}$	Flag	K$_S$/r
201059	<9.54	$0.46^{+0.00}_{-0.00}$	0.530 ± 0.014	0.828 ± 0.004	$0.00^{+0.00}_{-0.00}$	2.4195	0	r
207730	<9.58	$0.38^{+0.00}_{-0.11}$	0.343 ± 0.024	0.683 ± 0.003	$0.00^{+0.00}_{-0.00}$	1.7208	0	r
212767	$10.20^{+0.12}_{-0.20}$	$1.29^{+0.01}_{-0.00}$	1.406 ± 0.002	0.826 ± 0.003	$0.60^{+0.03}_{-0.06}$	1.8113*	0	K$_S$
423139	$10.92^{+0.00}_{-0.10}$	$2.17^{+0.01}_{-0.19}$	2.074 ± 0.000	0.897 ± 0.002	$1.60^{+0.10}_{-0.25}$	2.0277	0	K$_S$
423512	$10.45^{+0.00}_{-0.00}$	$1.80^{+0.00}_{-0.19}$	1.707 ± 0.001	0.041 ± 0.032	$1.80^{+0.05}_{-0.22}$	1.8690	0	K$_S$
417834	$10.41^{+0.00}_{-0.00}$	$1.22^{+0.00}_{-0.00}$	1.362 ± 0.002	1.267 ± 0.002	$0.20^{+0.00}_{-0.00}$	1.8480	0	K$_S$
417006	<9.42	$0.38^{+0.00}_{-0.00}$	0.442 ± 0.018	0.730 ± 0.003	$0.00^{+0.00}_{-0.00}$	2.1056	0	r
426641	$10.27^{+0.00}_{-0.00}$	$1.17^{+0.00}_{-0.00}$	1.212 ± 0.003	0.502 ± 0.006	$1.00^{+0.00}_{-0.00}$	1.9692	0	K$_S$
194583	$9.66^{+0.02}_{-0.18}$	$0.84^{+0.10}_{-0.10}$	0.969 ± 0.004	1.188 ± 0.003	$0.00^{+0.03}_{-0.00}$	1.8564	1	K$_S$
200822	$10.33^{+0.08}_{-0.19}$	$1.35^{+0.19}_{-0.01}$	1.458 ± 0.002	0.335 ± 0.032	$1.20^{+0.22}_{-0.10}$	1.8641	1	K$_S$
209510	$8.685^{+0.70}_{-0.60}$	$0.59^{+0.05}_{-0.06}$	0.691 ± 0.009	0.844 ± 0.011	$0.00^{+0.03}_{-0.00}$	2.2799	1	K$_S$
417708	$9.83^{+0.02}_{-0.18}$	$0.97^{+0.01}_{-0.01}$	1.095 ± 0.003	1.324 ± 0.003	$0.00^{+0.01}_{-0.00}$	1.9455	1	K$_S$
429106	<9.46	$-0.17^{+0.39}_{-0.00}$	-0.144 ± 0.129	0.153 ± 0.044	$0.00^{+0.52}_{-0.00}$	1.0286	1	r
427286	<9.38	$0.06^{+0.45}_{-0.05}$	0.096 ± 0.054	0.231 ± 0.038	$0.00^{+0.48}_{-0.00}$	2.3756	1	r
195048	$10.95^{+0.00}_{-0.00}$	$1.88^{+0.00}_{-0.00}$	2.234 ± 0.000	2.640 ± 0.000	$0.00^{+0.00}_{-0.00}$	x	2	K$_S$
194379	$10.63^{+0.00}_{-0.08}$	$1.96^{+0.00}_{-0.01}$	2.161 ± 0.000	1.349 ± 0.002	$0.80^{+0.03}_{-0.02}$	0.6573	2	K$_S$
198695	<9.64	$0.15^{+0.19}_{-0.00}$	0.254 ± 0.032	0.397 ± 0.012	$0.00^{+0.20}_{-0.00}$	0.2831	2	r
200702	$10.84^{+0.09}_{-0.00}$	$2.28^{+0.01}_{-0.01}$	2.321 ± 0.000	1.467 ± 0.001	$1.00^{+0.13}_{-0.12}$	0.9199	2	K$_S$
215533	$10.99^{+0.19}_{-0.17}$	$3.20^{+0.05}_{-0.19}$	3.151 ± 0.000	1.022 ± 0.002	$2.20^{+0.10}_{-0.10}$	1.2596*	2	K$_S$
423457	$10.42^{+0.00}_{-0.00}$	$1.80^{+0.00}_{-0.18}$	1.780 ± 0.001	0.458 ± 0.005	$1.60^{+0.06}_{-0.22}$	1.8387	2	K$_S$
422693	$10.43^{+0.00}_{-0.00}$	$1.30^{+0.01}_{-0.18}$	1.735 ± 0.001	1.339 ± 0.002	$0.20^{+0.03}_{-0.20}$	0.4392	2	K$_S$
420412	$10.67^{+0.00}_{-0.00}$	$2.60^{+0.03}_{-0.23}$	2.507 ± 0.000	0.304 ± 0.022	$2.40^{+0.14}_{-0.37}$	1.7594	2	K$_S$
416718	<9.59	$0.34^{+0.00}_{-0.00}$	0.356 ± 0.023	0.712 ± 0.004	$0.00^{+0.00}_{-0.00}$	1.1273	2	r
425717	<9.55	$0.74^{+0.22}_{-0.00}$	0.834 ± 0.008	0.640 ± 0.003	$0.60^{+0.20}_{-0.04}$	1.3557	2	r
210959	<9.50	$-0.001^{\dagger}$	-0.180 ± 0.337	0.248 ± 0.007	$0.00^{\dagger}$	x	2	r

Table of physical quantities of the Lyα emitters located in the Strazzullo protocluster. ID's are from the UltraVISTA catalog by Muzzin et al. [2013a], stellar masses are computed either from SED-fitting or using the mass-to-light ratio from Arnouts et al. [2007], the latter is 3σ upper limits. Star formation rates are obtained through SED-fitting and computed from UV- and Lyα-luminosities. Photometric redshifts are provided when available. Objects marked with a * have spectroscopic redshifts available: z$_{SPEC}$ = 2.1897 and 2.1460, respectively. Dust extinctions are found through SED-fitting and quality flags are assigned as described in Section 3.6. The object with ID: 210959 is not detected in the COSMOS 2015 catalog, nor in the UltraVISTA K_S-band selected catalog, thus SED-fitted results (marked with †) is extracted directly from the UltraVISTA r-band selected catalog, where no uncertainties are provided.

Table 4.2: Yuan Protocluster

ID	M_*^{TOT} [log(M$_\odot$)]	SFR_{CSF} [log(M$_\odot$/yr)]	SFR_{UV}^{TOT} [log(M$_\odot$/yr)]	$SFR_{Ly\alpha}^{TOT}$ [log(M$_\odot$/yr)]	A_V [mag]	z_{PHOT}	Flag	K_S/r
355771	<9.544	$0.81^{+0.00}_{-0.00}$	0.874 ± 0.006	1.207 ± 0.003	$0.00^{+0.00}_{-0.00}$	2.0058*	0	r
356891	<9.583	$1.72^{+0.01}_{-0.18}$	1.715 ± 0.001	0.650 ± 0.010	$1.20^{+0.14}_{-0.20}$	1.8889	0	K_S
357136	$10.198^{+0.12}_{-0.20}$	$1.63^{+0.17}_{-0.02}$	1.471 ± 0.003	0.378 ± 0.017	$1.80^{+0.26}_{-0.09}$	2.1571	0	K_S
361824	$10.922^{+0.00}_{-0.10}$	$0.12^{+0.11}_{-0.00}$	0.197 ± 0.038	0.461 ± 0.006	$0.00^{+0.09}_{-0.00}$	1.8015	0	r
380280	$10.445^{+0.00}_{-0.00}$	$0.87^{+0.00}_{-0.00}$	0.921 ± 0.005	1.250 ± 0.001	$0.00^{+0.00}_{-0.00}$	2.0315*	0	K_S
379139	$10.414^{+0.00}_{-0.00}$	$1.95^{+0.01}_{-0.00}$	1.964 ± 0.000	1.454 ± 0.001	$0.80^{+0.02}_{-0.01}$	1.8401*	0	K_S
377883	<9.421	$0.32^{+0.19}_{-0.00}$	0.388 ± 0.024	0.517 ± 0.012	$0.20^{+0.20}_{-0.00}$	1.7386	0	r
357737	$10.273^{+0.00}_{-0.00}$	$0.68^{+0.04}_{-0.00}$	0.735 ± 0.009	0.575 ± 0.018	$0.40^{+0.07}_{-0.07}$	2.1757	1	K_S
361634	$9.658^{+0.02}_{-0.18}$	$0.98^{+0.00}_{-0.00}$	0.946 ± 0.007	0.501 ± 0.016	$0.80^{+0.00}_{-0.00}$	2.1321	1	K_S
362975	$10.332^{+0.08}_{-0.19}$	$1.88^{+0.19}_{-0.00}$	1.874 ± 0.001	0.806 ± 0.012	$1.40^{+0.20}_{-0.05}$	1.8564	1	K_S
370558	$8.685^{+0.70}_{-0.60}$	$-0.08^{+0.19}_{-0.00}$	-0.028 ± 0.081	0.180 ± 0.042	$0.00^{+0.20}_{-0.00}$	1.6168	1	r
380267	$9.825^{+0.02}_{-0.18}$	$0.54^{+0.15}_{-0.18}$	0.545 ± 0.015	0.635 ± 0.015	$0.20^{+0.21}_{-0.20}$	1.8905	1	r
377222	<9.458	$0.57^{+0.00}_{-0.00}$	0.578 ± 0.012	1.012 ± 0.007	$0.00^{+0.00}_{-0.00}$	1.7673	1	r
377035	<9.379	$0.46^{+0.00}_{-0.00}$	0.561 ± 0.013	0.788 ± 0.010	$0.00^{+0.00}_{-0.00}$	2.0001	1	K_S
380231	<9.379	$2.58^{+0.19}_{-0.00}$	2.576 ± 0.000	0.897 ± 0.003	$1.80^{+0.21}_{-0.12}$	1.8095	2	K_S

Table of physical quantities of the Lyα emitters located in the Yuan protocluster. ID's are from the UltraVISTA catalog by Muzzin et al. [2013a], stellar masses are computed either from SED-fitting or using the mass-to-light ratios from Arnouts et al. [2007], the latter is 3σ upper limits. Star formation rates are obtained through SED-fitting and computed from UV- and Lyα-luminosities. Photometric redshifts are also provided. Objects marked with a * have spectroscopic redshifts available: $z_{SPEC} = 2.094$, 2.098, and 2.097, respectively. Dust extinctions are found through SED-fitting and quality flags are assigned as described in Section 3.6.

4.6 Extended Lyman-alpha Emission

Apart from examining how the surrounding environments affect galaxy evolution, this thesis is also aimed at investigating the presence of extended Lyα emission within protocluster environments. The galaxy clusters we observe today are often associated with large reservoirs of superheated gas, detected through X-ray emission (see e.g. Sarazin [1986] and references therein). However, the feedback mechanisms driving the cooling or heating of the intracluster medium (ICM) are still not fully understood.
While no extended X-ray emission is detected within either of the Strazzullo or Yuan protoclusters, gas might still be present in their ICM. The population of galaxies in clusters at z$\sim$0 are dominated by quiescent objects, while at higher redshift we expect the fraction of star-forming galaxies to increase. The star formation history of our universe shows a peak in star formation around z$\sim$2 [Madau & Dickinson, 2014], thus we expect to observe a larger fraction of star-forming galaxies at this redshift. As the Strazzullo and Yuan protoclusters are observed to be at redshifts 2.19 and 2.095, respectively, we would also expect to see a larger number of star-forming galaxies in these protoclusters, compared to local galaxy clusters. Since star formation is dependent on cold gas, continuous star formation in cluster- or protocluster galaxies might indicate that large amounts of cold gas are available in the ICM, feeding new gas to the star-forming galaxies. This gas will not have been heated to the extent that it emits X-ray emission. However, ionizing photons, originating from newly formed stars or AGN within the protocluster galaxies, can excite the ICM, resulting in Lyα emission [Valentino et al., 2016].
If cold Lyα emitting gas were present in the Strazzullo or Yuan protoclusters, we should have been able to detect it with the narrow-band filters used for obtaining the observations of the two protoclusters. However, when inspecting the reduced science frames of each protocluster, we see no evidence for extended reservoirs of Lyα emitting gas in the central regions of the protocluster. This indicates that extended reservoirs of ionized gas are not present within the protoclusters, down to our limiting surface brightness. While we do not detect any giant extended Lyα emission in the ICM, gas reservoirs might still be present, though further observations are needed to investigate whether this is the case.

5 Future Perspectives

The sample we obtain of Lyα emitting protocluster galaxies allow for investigating the physical properties of such galaxies, as well as how these might be affected by their surrounding environment. However, as previously mentioned, this study is limited, amongst other things, by low number statistics. In this section we contemplate how we can improve the sample of Lyα emitters, as well as propose ideas for follow-up observations of specific objects. We also describe in further detail a QSO pair that we have discovered in the Strazzullo protocluster, along with the research potential of this finding.

5.1 Follow-up Observations

The narrow-band imaging technique used in this work has allowed us to build a catalog of protocluster galaxies with well-detected Lyα emission. This catalog contains estimates of stellar mass, star formation rates, dust extinction and photometric redshifts. However, we find it interesting not only to be able to impose further constraints on the above quantities, but also to expand this catalog of Lyα emitters.

As evident from Tables 4.1 and 4.2, spectroscopic redshifts are only available for very few of our sample galaxies. Besides from obtaining accurate measurements of redshift, and thereby distance, spectral features can be used for obtaining parameters such as SFR. Hence, spectroscopic observations are a powerful tool for achieving more accurate measurements of the physical parameters of galaxies. We would like to obtain spectroscopy for at least some of our detected Lyα emitters. Spectroscopic confirmation of redshifts for our sample of Lyα emitters is of great interest to us, as this would provide further evidence that these are indeed members of the Strazzullo and Yuan protoclusters. We also hope that analysis of spectral features will contribute with additional information about parameters such as SFR, M_* and dust content of the observed galaxies.

In practice, it could be interesting to confirm the Lyα emission lines of the detected emitters, e.g., using the FORS2 multislit spectrograph at the Very Large Telescope. Moreover, by spectroscopically confirming spectral lines such as Hα or Hβ with near-IR spectrographs, we would be able to better trace the SFR in the Lyα emitting galaxies. With spectrographs, such as MOSFIRE at the Keck telescope, MOIRCS at the Subaru telescope, or KMOS at ESO/VLT, it would also be possible to explore the metallicity of the emitters or to look further into AGN activity.

We find two candidates in our catalog of Lyα emitters for which we are especially interested in obtaining spectroscopic measurements. One is an object, ID:210959[3], which is barely visible in the CFHT u-band image, but is well-detected in the narrow-band frame. We fail to locate this object in the COSMOS 2015 catalog, but are able to find it in the UltraVISTA r-band selected catalog. The other object, ID:215533, is a galaxy of $M_* \sim 10^{11} M_\odot$ with an estimated extinction of about 2 magnitudes and a surprisingly high SFR compared to what is expected from the galactic main sequence. We find it interesting that we detect Lyα emission from this object, as we would expect all Lyα photons to be absorbed by dust, which is why we would like to investigate this galaxy further. If we were able to get spectroscopic confirmation of Lyα and Hα lines for this object, we could establish the nature of the starburst and derive the Lyα escape fraction of this galaxy. Furthermore, it might also be possible to relate this to the distribution of dust in the galaxy to establish if the starburst might be due to a merger event.

Another reason for which we would like to obtain further observations of our Lyα emitters is to improve the depth of the observations currently available. As we also mentioned in Section 4.2, our results are both limited by low number statistics, but also by the limiting flux. If we were able to achieve deeper narrow-band observations, e.g., by increasing the number of exposures of the protocluster fields, this would likely result in a larger number of detected Lyα emitters. Hence, we would be provided with better statistics and would also be able to determine how the number counts of our Lyα emitters change at lower flux levels. However, in order to obtain a fully representative sample of Lyα emitting protocluster galaxies, narrow-band observations of several other protocluster candidates are also required.

5.2 A QSO Pair in the Strazzullo Protocluster

Though we do not find evidence of any giant extended Lyα emission in the ICM of the Strazzullo or Yuan protoclusters, we do find evidence of extended Lyα emission in the periphery of the Strazzullo protocluster.
This Lyα blob (LAB) is located between two of the detected Lyα emitters, both of which have been confirmed to be AGN, being detected in deep Chandra X-ray images [Civano et al., 2016]. The nature of the LAB is still uncertain, but it might be caused by outflows from one or both of these active galaxies, or representing gas in the circumgalactic medium surrounding these two massive objects. Following the identification of the giant LAB from the analysis presented in this thesis, two members of our collaboration, Dr. Emanuele Daddi (CEA Saclay) and Prof. Mike Rich (UCLA), proposed, obtained, and carried out follow-up spectroscopy of this

[3]ID from the UltraVISTA catalog by Muzzin et al. [2013a]

system with the Keck Cosmic Web Imager instrument (KCWI, Morrissey et al. [2018]) on the Keck Telescope, confirming the redshift of the two AGN and the existence of the LAB. Figure 5.1 shows the Lyα emission map of the system, where we initially detect the LAB, alongside the same region extracted from the spectral cube obtained with the Keck Telescope.
The extent of the Lyα emission between the two AGN are approximately 8.27 arcseconds, corresponding to ~68 kpc at the redshift z=2.19 of the system. Figure 5.2 shows a map of the region around the two AGN, as well as a colour image with contours of the Lyα emission. As previously mentioned, both AGN are detected Lyα emitters. However, as can also be seen on Figure 5.2, the AGN are also classified as massive objects. The southernmost galaxy is classified as being star-forming, while the northernmost is classified as quiescent. The colour image of the region surrounding the AGN shows both galaxies as red objects, but it also reveals a few surrounding galaxies, one of which shows a similar colour and is a massive candidate member with a photometric redshift consistent with the one of the AGN pair and the Strazzullo protocluster. The remaining objects are likely interlopers. We are investigating the rich information included in the KCWI spectral cube, in order to possibly confirm the redshifts of several other galaxies in the field of view.

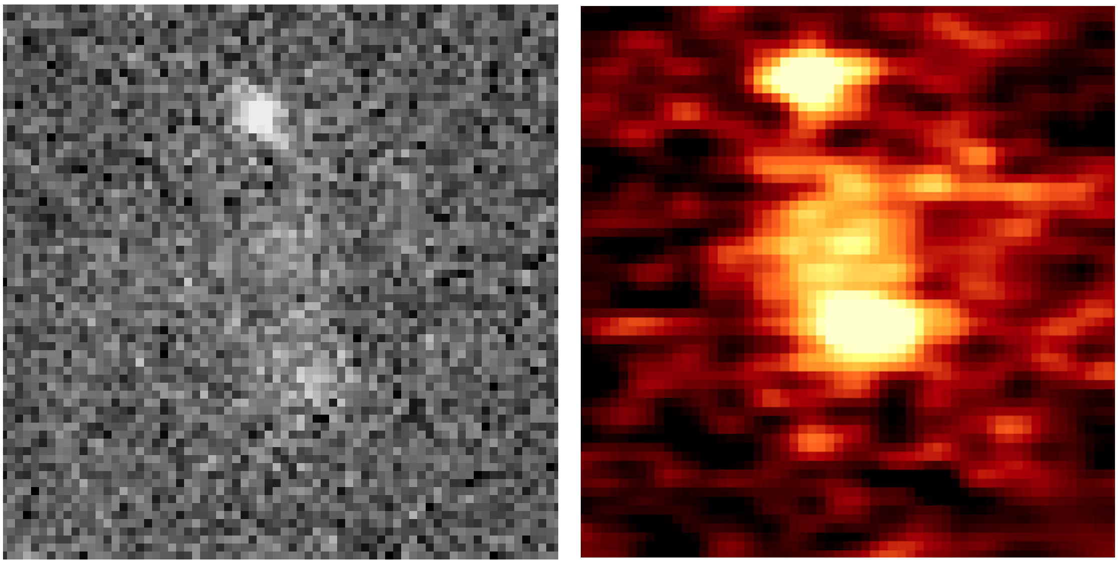

Figure 5.1: Lyα emission map and spectrum of the QSO pair and the LAB. Shown on the left is the Lyα emission map, in which we first detected the two AGN and the extended emission between them. On the right is an image created from the spectral cube obtained by Dr. Emanuele Daddi (CEA Saclay) and Prof. Mike Rich (UCLA), where information is extracted in the x,y plane around the wavelength covering Lyα at z=2.19.

The spectral cube obtained with the KCWI instrument contains three dimensions: position (x,y) and wavelength. As we have been given access to the reduced

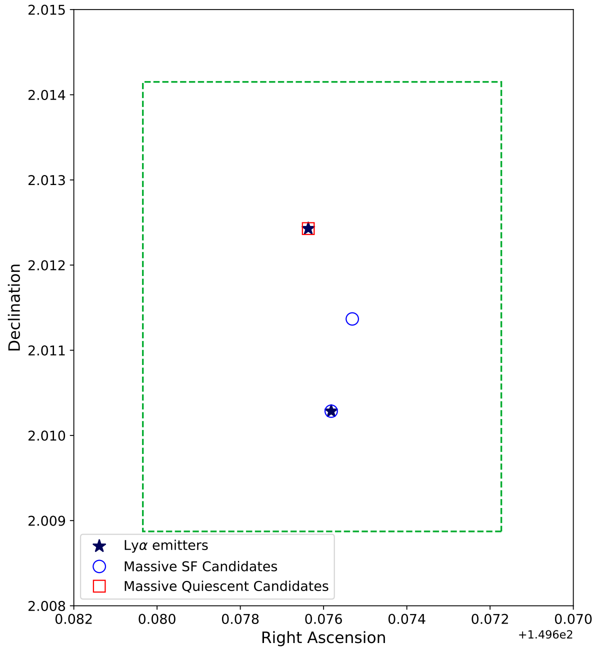

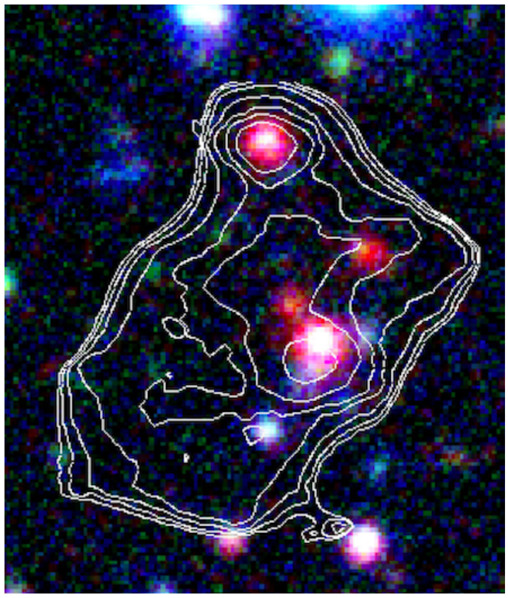

Figure 5.2: Maps showing the AGN-pair we discover in the Strazzullo protocluster. The left panel is a zoom of Figure 4.1, showing the position of the two AGN. The right panel shows a colour image of the area around the AGN, aling with contours of the extended emission, obtained by Dr. Emanuele Daddi (CEA Saclay) and Prof. Mike Rich (UCLA). The spectoscopic data from the KCWI instrument on the Keck Telescope covers the area surrounding the AGN pair, including the giant extended Lyα emission between these.

spectral data [E. Daddi, private communication], we are able to obtain a 'slice' or an image of the region covered by the spectra, as the one shown in the right panel of Figure 5.1, by extracting data at a specific wavelength. If, on the other hand, data is extracted along the wavelength axis, a one-dimensional spectrum can be produced, making it possible for us to explore the spectra of the two AGN and the Lyα emitting region between them. We show these spectra in Figure 5.3. The Lyα emission line is clearly visible in all three spectra, confirming that these are indeed Lyα emitters. Emission from CIV and HeII also seem to be present, especially for the northernmost AGN (top panel on Figure 5.3). The southernmost AGN (bottom panel) does not have as strong HeII emission, and the CIV lines seem to show some signs of absorption. The LAB between the AGN, on the other hand, has an absence of CIV and HeII emission, suggesting that the gas might be metal poor, which is not consistent with material from outflows, but is more likely the circumgalactic medium.

Different Lyα line profiles seem to be present in the three spectra. The northernmost AGN has the widest emission line, suggesting the possible presence of strong outflows. The LAB spectrum seem to be showing a double line profile due to rotation in the gas, or more likely, radiative transfer effects [Dijkstra, 2017, Verhamme et al., 2006].

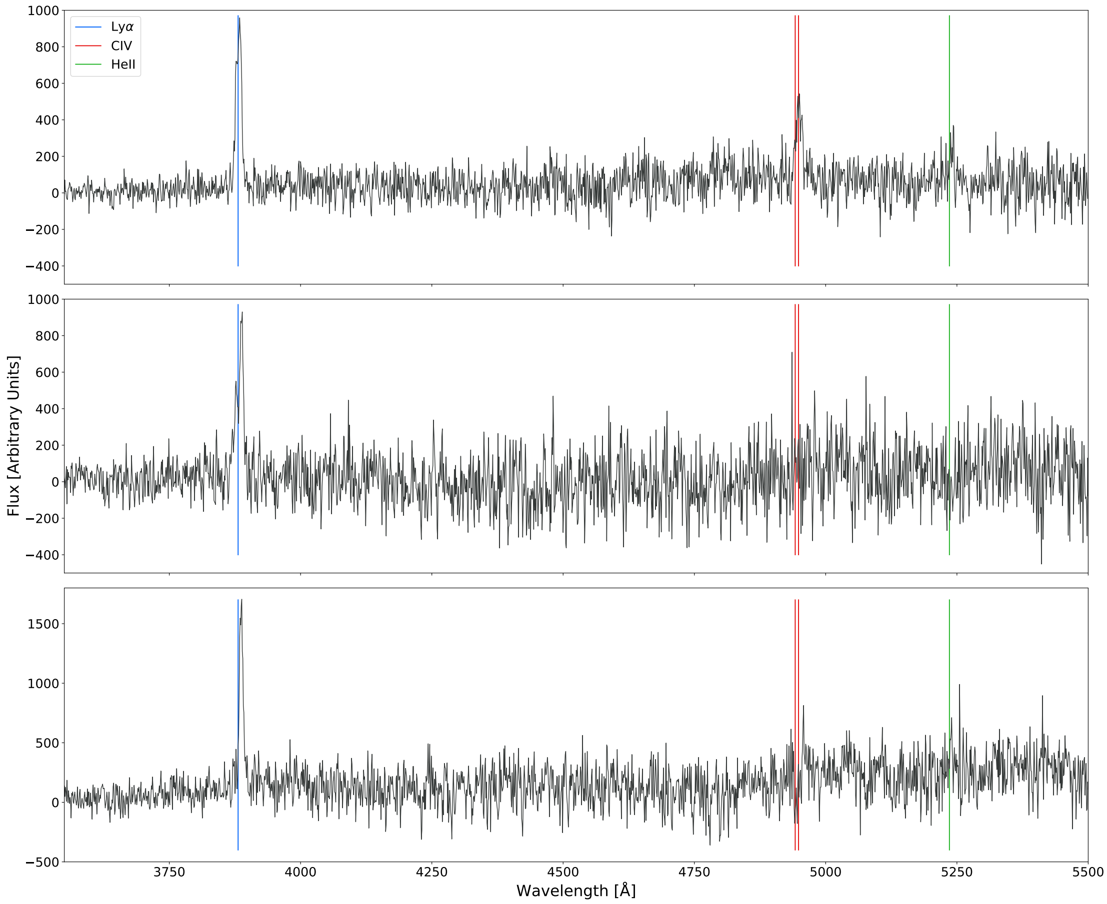

Figure 5.3: Spectra of the QSO system. Top panel is the spectrum of the northernmost AGN, middle panel is the spectrum of the Lyα blob between the two AGN, and bottom panel is the spectrum of the southernmost AGN. Positions of Lyα-, CIV, and HeII emission lines are marked with blue, red, and green lines, respectively. From these spectra it is clear that the LAB has a more complex Lyα profile than the two AGN and that there is an absence of CIV and HeII in this nebula.

AGN are not a rarity within galaxy clusters. However, pairs of AGN are not as often observed in these environments. It has been suggested that small-scale clustering of QSOs might be caused by interaction between the host galaxies, though it has still not been determined whether this is the case.
The preliminary analysis of the QSO pair and the LAB suggests that this is a complex and interesting system, which we would like to explore even further. As mentioned earlier, emission line profiles would provide valuable information on the nature of the emitting gas, such as, e.g., densities and whether some of the material might originate from in- or outflows from the two AGN. By investigating these data, we should also be able to extract information about the luminosity of the Lyα emission and the velocity of the gas within the giant Lyα nebula. The

information available from the spectral data could possibly help determine whether this system is connected with the formation of structure and provide some insight as to why the QSO-pair is located in the periphery, and not in the central part, of the protocluster. These spectral data do indeed contain a large amount of information about this system, and thus, we have just scratched the surface by confirming the presence of the LAB and the redshift of the system.

6 Conclusions

In this thesis we have presented the results of a VLT/FORS2 narrow-band imaging campaign, which targets two protoclusters of galaxies at z$\sim$2, in order to detect Lyα emission. We find that the narrow-band imaging technique is a powerful method for isolating objects with significant narrow-band excess over large portions of the sky with a relatively cheap time expense. We build a sample of Lyα emitters containing a total of 40 galaxies, all part of the COSMOS 2015 and UltraVISTA K_S- or r-band selected catalogs. These galaxies have significant detections in Lyα, as well as photometric redshifts roughly consistent with the systemic redshifts of the Strazzullo and Yuan protoclusters (2.19 and 2.095, respectively). We derive stellar masses from SED-fitting and mass-to-light ratios and compute star formation rates from UV- and Lyα luminosities. These parameters are then compared to the main sequence of galaxies [Sargent et al., 2014]. The detected Lyα emitters cover a wide range of stellar masses and star formation rates (see Tables 4.1 and 4.2). Thus, we find that our sample of Lyα emitters are not representing a homogeneous population of galaxies.

The majority of our protocluster Lyα emitters is located below the main sequence of field galaxies, having star formation rates lower than expected for their stellar mass. When we compare the projected number counts of our protocluster sample to values derived from general Lyα luminosity functions at similar redshifts, we find lower number counts than anticipated within 1 Mpc from the protocluster centers, but fully consistent trends within $\leq$2 Mpc, when approaching field-like densities. These results suggest that Lyα emitting protocluster galaxies are indeed affected by the surrounding environment, possibly leading these galaxies to become quiescent earlier than expected for similar counterparts in the field. We suggest that Lyα emission might not be suitable as tracer of massive, and relatively evolved, galaxy overdensities at z$\sim$2, as we do not find an overdensity of Lyα emitters in either of the two protoclusters we investigate, down to our limiting Lyα flux. Neither do we find evidence of extended Lyα emission in the protocluster cores, indicating that large reservoirs of ionized gas are not present in the intracluster medium of the Strazzullo and Yuan protoclusters. However, we do find a Lyα blob located between two AGN in the periphery of the Strazzullo protocluster. This LAB and this rare QSO-pair are currently being investigated further through follow-up spectroscopy.

Our results indicate that protocluster galaxies are indeed affected by their surrounding environment. However, further observations of Lyα emitting galaxies are needed, in order to confirm these results and obtain better number statistics.

Bibliography

Arnouts, S., Walcher, C. J., Le Fèvre, O., et al. 2007, *Astron. & Astrophys.*, 476, 137

Balogh, M. L., Baldry, I. K., Nichol, R., et al. 2004, *Astrophys. J. Lett.*, 615, L101

Bertin, E., & Arnouts, S. 1996, *Astron. & Astrophys.* Supplement, 117, 393

Bertin, E., Mellier, Y., Radovich, M., et al. 2002, in Astronomical Society of the Pacific Conference Series, Vol. 281, Astronomical Data Analysis Software and Systems XI, ed. D. A. Bohlender, D. Durand, & T. H. Handley, 228

Brinchmann, J., Charlot, S., White, S. D. M., et al. 2004, *Mon. Not. R. Astron. Soc.*, 351, 1151

Bruzual, G., & Charlot, S. 2003, *Mon. Not. R. Astron. Soc.*, 344, 1000

Bunker, A. J., Warren, S. J., Hewett, P. C., & Clements, D. L. 1995, *Mon. Not. R. Astron. Soc.*, 273, 513

Bussmann, R. S., Riechers, D., Fialkov, A., et al. 2015, *Astrophys. J.*, 812, 43

Calzetti, D., Armus, L., Bohlin, R. C., et al. 2000, *Astrophys. J.*, 533, 682

Chabrier, G. 2003, The Publications of the Astronomical Society of the Pacific, 115, 763

Civano, F., Marchesi, S., Comastri, A., et al. 2016, *Astrophys. J.*, 819, 62

Colless, M., Dalton, G., Maddox, S., et al. 2001, *Mon. Not. R. Astron. Soc.*, 328, 1039

Daddi, E., Cimatti, A., Renzini, A., et al. 2004, *Astrophys. J.*, 617, 746

Daddi, E., Dickinson, M., Morrison, G., et al. 2007, *Astrophys. J.*, 670, 156

Dijkstra, M. 2017, arXiv e-prints, arXiv:1704.03416

Dressler, A. 1980, *Astrophys. J.*, 236, 351

Elbaz, D., Daddi, E., Le Borgne, D., et al. 2007, *Astron. & Astrophys.*, 468, 33

Gawiser, E., Francke, H., Lai, K., et al. 2007, *Astrophys. J.*, 671, 278

Girardi, M., Biviano, A., Giuricin, G., Mardirossian, F., & Mezzetti, M. 1993, *Astrophys. J.*, 404, 38

Gobat, R., Daddi, E., Onodera, M., et al. 2011, *Astron. & Astrophys.*, 526, A133

Gobat, R., Daddi, E., Coogan, R. T., et al. 2019, arXiv e-prints, arXiv:1907.10985

Gómez-Guijarro, C., Toft, S., Karim, A., et al. 2018, *Astrophys. J.*, 856, 121

Gómez-Guijarro, C., Riechers, D. A., Pavesi, R., et al. 2019, *Astrophys. J.*, 872, 117

Gott, J. Richard, I., Melott, A. L., & Dickinson, M. 1986, *Astrophys. J.*, 306, 341

Gunn, J. E., & Gott, J. Richard, I. 1972, *Astrophys. J.*, 176, 1

Hayes, M., Schaerer, D., Östlin, G., et al. 2011, *Astrophys. J.*, 730, 8

Hayes, M., Östlin, G., Schaerer, D., et al. 2010, *Nature*, 464, 562

Hubble, E. P. 1926, *Astrophys. J.*, 64, 321

Jiang, L., Wu, J., Bian, F., et al. 2018, Nature Astronomy, 2, 962

Kacprzak, G. G., Yuan, T., Nanayakkara, T., et al. 2015, *Astrophys. J. Lett.*, 802, L26

Kennicutt, Robert C., J. 1998, *Annu. Rev. Astron. Astrophys.*, 36, 189

Kewley, L. J., Yuan, T., Nanayakkara, T., et al. 2016, *Astrophys. J.*, 819, 100

Konno, A., Ouchi, M., Nakajima, K., et al. 2016, *Astrophys. J.*, 823, 20

Kravtsov, A. V., & Borgani, S. 2012, *Annu. Rev. Astron. Astrophys.*, 50, 353

Laigle, C., McCracken, H. J., Ilbert, O., et al. 2016, *Astrophys. J. Suppl. Series*, 224, 24

Larson, R. B., Tinsley, B. M., & Caldwell, C. N. 1980, *Astrophys. J.*, 237, 692

Lilly, S. J., Le Fèvre, O., Renzini, A., et al. 2007, *Astrophys. J. Suppl. Series*, 172, 70

Madau, P., & Dickinson, M. 2014, *Annu. Rev. Astron. Astrophys.*, 52, 415

Magdis, G. E., Daddi, E., Béthermin, M., et al. 2012, *Astrophys. J.*, 760, 6

McCracken, H. J., Milvang-Jensen, B., Dunlop, J., et al. 2012, *Astron. & Astrophys.*, 544, A156

Milvang-Jensen, B., Freudling, W., Zabl, J., et al. 2013, *Astron. & Astrophys.*, 560, A94

Morrissey, P., Matuszewski, M., Martin, D. C., et al. 2018, *Astrophys. J.*, 864, 93

Muzzin, A., Marchesini, D., Stefanon, M., et al. 2013a, *Astrophys. J. Suppl. Series*, 206, 8

—. 2013b, *Astrophys. J.*, 777, 18

Noeske, K. G., Weiner, B. J., Faber, S. M., et al. 2007, *Astrophys. J. Lett.*, 660, L43

Oesch, P. A., Brammer, G., van Dokkum, P. G., et al. 2016, *Astrophys. J.*, 819, 129

Osterbrock, D. E., & Ferland, G. J. 2006, Astrophysics of Gaseous Nebulae and Active Galactic Nuclei

Overzier, R. A. 2016, The *Astron. & Astrophys.*Review, 24, 14

Price-Whelan, A. M., Sipőcz, B. M., Günther, H. M., et al. 2018, The Astronomical Journal, 156, 123

Ryden, B. 2003, Introduction to Cosmology

Salpeter, E. E. 1955, *Astrophys. J.*, 121, 161

Sarazin, C. L. 1986, Reviews of Modern Physics, 58, 1

Sargent, M. T., Daddi, E., Béthermin, M., et al. 2014, *Astrophys. J.*, 793, 19

Schreiber, C., Pannella, M., Elbaz, D., et al. 2015, *Astron. & Astrophys.*, 575, A74

Scoville, N., Aussel, H., Brusa, M., et al. 2007, *Astrophys. J. Suppl. Series*, 172, 1

Sobral, D., & Matthee, J. 2019, *Astron. & Astrophys.*, 623, A157

Sobral, D., Matthee, J., Best, P., et al. 2017, *Mon. Not. R. Astron. Soc.*, 466, 1242

Sparke, L. S., & Gallagher, John S., I. 2007, Galaxies in the Universe

Speagle, J. S., Steinhardt, C. L., Capak, P. L., & Silverman, J. D. 2014, *Astrophys. J. Suppl. Series*, 214, 15

Spitler, L. R., Labbé, I., Glazebrook, K., et al. 2012, *Astrophys. J. Lett.*, 748, L21

Spitzer, L. 1978, Physical Processes in the Interstellar Medium, doi:10.1002/9783527617722

Strazzullo, V., Daddi, E., Gobat, R., et al. 2015, *Astron. & Astrophys.*, 576, L6

Sunyaev, R. A., & Zeldovich, Y. B. 1970, Comments on Astrophysics and Space Physics, 2, 66

Tacconi, L. J., Genzel, R., Saintonge, A., et al. 2018, *Astrophys. J.*, 853, 179

Tody, D. 1986, in Society of Photo-Optical Instrumentation Engineers (SPIE) Conference Series, Vol. 627, Instrumentation in astronomy VI, ed. D. L. Crawford, 733

Toft, S., Smolčić, V., Magnelli, B., et al. 2014, *Astrophys. J.*, 782, 68

Valentino, F., Daddi, E., Strazzullo, V., et al. 2015, *Astrophys. J.*, 801, 132

Valentino, F., Daddi, E., Finoguenov, A., et al. 2016, *Astrophys. J.*, 829, 53

van Dokkum, P. G. 2001, Publications of the Astronomical Society of the Pacific, 113, 1420

Venemans, B. P., Röttgering, H. J. A., Miley, G. K., et al. 2005, *Astron. & Astrophys.*, 431, 793

—. 2007, *Astron. & Astrophys.*, 461, 823

Verhamme, A., Schaerer, D., & Maselli, A. 2006, *Astron. & Astrophys.*, 460, 397

Vogelsberger, M., Genel, S., Springel, V., et al. 2014, *Mon. Not. R. Astron. Soc.*, 444, 1518

Wang, T., Elbaz, D., Daddi, E., et al. 2016, *Astrophys. J.*, 828, 56

Williams, R. J., Quadri, R. F., Franx, M., van Dokkum, P., & Labbé, I. 2009, *Astrophys. J.*, 691, 1879

Wuyts, S., Labbé, I., Franx, M., et al. 2007, *Astrophys. J.*, 655, 51

Yuan, T., Nanayakkara, T., Kacprzak, G. G., et al. 2014, *Astrophys. J. Lett.*, 795, L20

Zwicky, F. 1933, Helvetica Physica Acta, 6, 110

A SEDs of non-Ks Detected Emitters

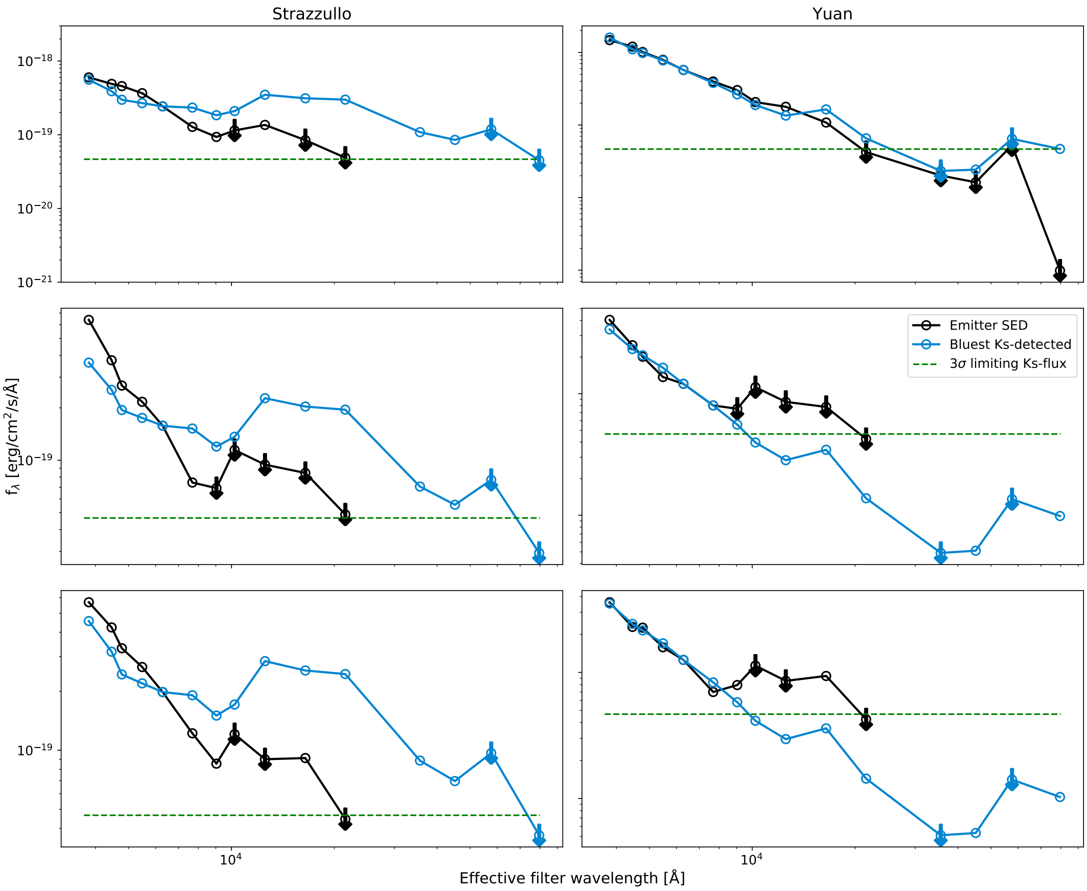

Figure A.1: SEDs of non-K_S detected Lyα emitters with quality flag 0 (black). The bluest available SED of the Lyα emitters detected in the K_S-band (blue), for each protocluster, has been rescaled to the r-band flux level of the non-K_S detected emitter SEDs. The green, dashed line shows the 3σ limit on the K_S-band flux.

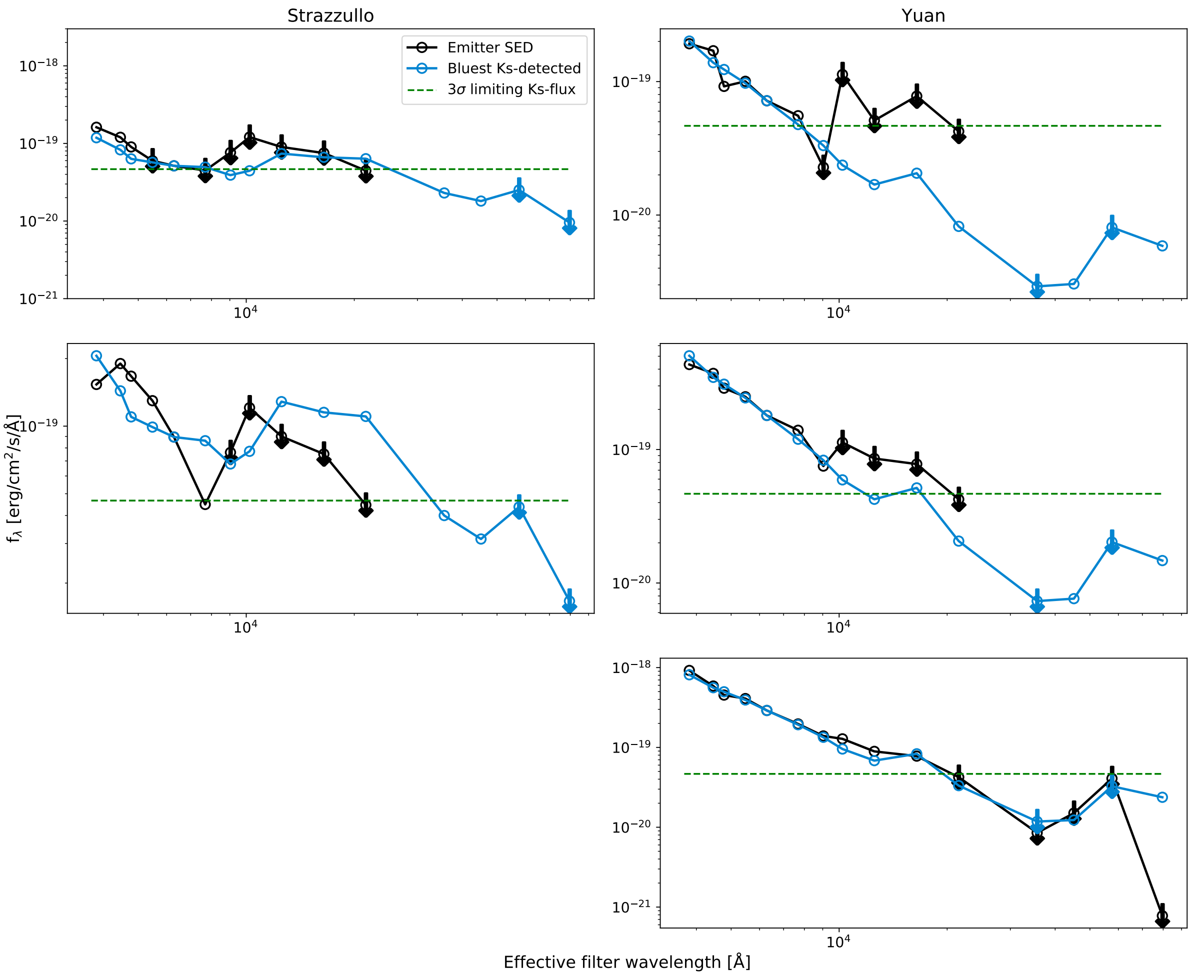

Figure A.2: SEDs of non-K_S detected Lyα emitters with quality flag 1 (black). The bluest available SED of the Lyα emitters detected in the K_S-band (blue), for each protocluster, has been rescaled to the r-band flux level of the non-K_S detected emitter SEDs. The green, dashed line shows the 3σ limit on the K_S-band flux.

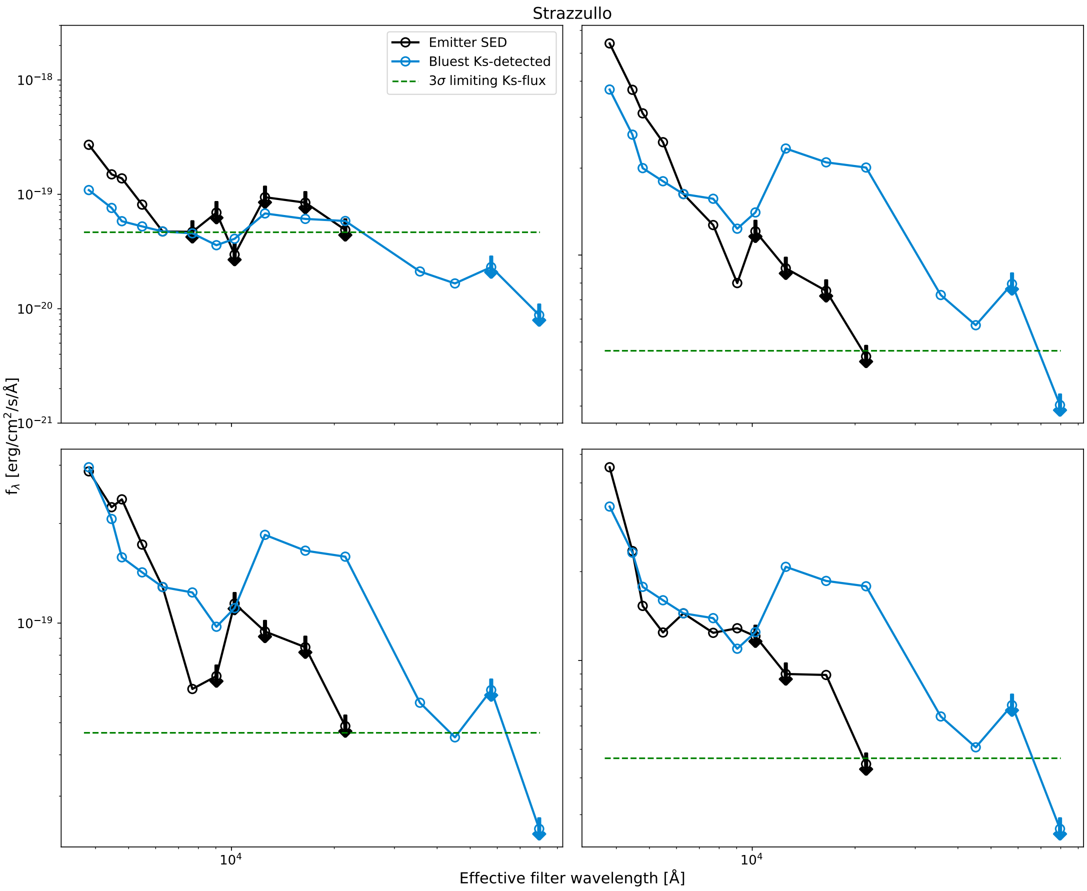

Figure A.3: SEDs of non-K_S detected Lyα emitters with quality flag 2 (black). The bluest available SED of the Lyα emitters detected in the K_S-band (blue), for each protocluster, has been rescaled to the r-band flux level of the non-K_S detected emitter SEDs. The green, dashed line shows the 3σ limit on the K_S-band flux.